European Journal of Pharmaceutics and Biopharmaceutics 179 (2022) 11–25

Contents lists available at ScienceDirect

European Journal of Pharmaceutics and Biopharmaceutics

journal homepage: www.elsevier.com/locate/ejpb

Biodistribution and toxicity of innate defense regulator 1018 (IDR-1018)

Tullio V.F. Esposito [a,b], Cristina Rodríguez-Rodríguez [a,c], Colin Blackadar [a], Evan F. Haney [d,e], Daniel Pletzer [f,*], Robert E.W. Hancock [d], Katayoun Saatchi [a], Urs O. Häfeli [a,b]

[a] Faculty of Pharmaceutical Sciences, University of British Columbia, Vancouver, Canada
[b] Department of Pharmacy, Faculty of Health and Medical Sciences, University of Copenhagen, Copenhagen, Denmark
[c] Department of Physics and Astronomy, Faculty of Science, University of British Columbia, Vancouver, Canada
[d] Centre for Microbial Disease and Immunity Research, Department of Microbiology and Immunology, Faculty of Science, University of British Columbia, Vancouver, Canada
[e] Asep Medical Holdings, Victoria, BC, Canada
[f] Department of Microbiology and Immunology, University of Otago, Dunedin, New Zealand

ARTICLE INFO

Keywords:
Pharmacokinetics
SPECT/CT
Isotope
Nuclear imaging
Radiotracer
Host defence peptide

ABSTRACT

Innate defense regulators (IDRs) are synthetic host-defense peptides (HDPs) with broad-spectrum anti-infective properties, including immunomodulatory, anti-biofilm and direct antimicrobial activities. A lack of pharmacokinetic data about these peptides hinders their development and makes it challenging to fully understand how they work *in vivo* since their mechanism of action is dependent on tissue concentrations of the peptide. Here, we set out to define in detail the pharmacokinetics of a well-characterized IDR molecule, IDR-1018. To make the peptide traceable, it was radiolabeled with the long-lived gamma-emitting isotope gallium-67. After a series of bench-top characterizations, the radiotracer was administered to healthy mice intravenously (IV) or subcutaneously (SQ) at various dose levels (2.5–13 mg/kg). Nuclear imaging and *ex-vivo* biodistributions were used to quantify organ and tissue uptake of the radiotracer over time. When administered as an IV bolus, the distribution profile of the radiotracer changed as the dose was escalated. At 2.5 mg/kg, the peptide was well-tolerated, poorly circulated in the blood and was cleared predominantly by the reticuloendothelial system. Higher doses (7 and 13 mg/kg) as an IV bolus were almost immediately lethal due to respiratory arrest; significant lung uptake of the radiotracer was observed from nuclear scans of these animals, and histological examination found extensive damage to the pulmonary vasculature and alveoli. When administered SQ at a dose of 3 mg/kg, radiolabeled IDR-1018 was rapidly absorbed from the site of injection and predominately cleared renally. Apart from the SQ injection site, no other tissue had a concentration above the minimum inhibitory concentration that would enable this peptide to exert direct antimicrobial effects against most pathogenic bacteria. Tissue concentrations were sufficient, however, to disrupt microbial biofilms and alter the host immune response. Overall, this study demonstrated that the administration of synthetic IDR peptide *in vivo* is best suited to local administration which avoids some of the issues associated with peptide toxicity that are observed when administered systemically by IV injection, an issue that will have to be addressed through formulation.

1. Introduction

Host defense peptides (HDPs) are short (~12–50 amino acid residues), amphipathic, cationic peptides with diverse activity ranging from antimicrobial and anti-biofilm to immune modulation. HDPs are produced by various cells and tissues in all complex life forms and function as a fundamental component of the innate immune system [1,2]. Over the last couple of decades, there has been a concerted effort to modify naturally occurring HDPs into synthetic peptides with enhanced immunomodulatory properties [3]. Some of these synthetic versions of HDPs have been termed innate defense regulators (IDRs), with IDR-1018 being one of the more promising and well-characterized compounds [4].

IDR-1018 (VRLIVAVRIWRR-NH_2) is loosely based on the sequence of Bac2a (RLARIVVIRVAR-NH_2) which itself represents the linearized form of the natural bovine HDP bactenecin in which the two disulphide forming Cys residues have been replaced by Ala residues [4]. IDR-1018 was selected from a library of Bac2a derivatives due to its enhanced ability to induce chemokine expression, such as MCP-1, from human

* Corresponding author.
E-mail address: daniel.pletzer@otago.ac.nz (D. Pletzer).

https://doi.org/10.1016/j.ejpb.2022.08.004
Received 21 May 2022; Received in revised form 3 August 2022; Accepted 10 August 2022
Available online 24 August 2022

peripheral blood mononuclear cells (PBMCs) [5]. Further *in vitro* studies using human neutrophils found that IDR-1018 i) suppressed the LPS-mediated production of reactive oxygen species (ROS) and proinflammatory cytokines like TNF-α, ii) promoted the release of the endogenous HDP LL-37 from neutrophil granules and iii) enhanced neutrophil adhesion to endothelial cells and promotes cell migration [6]. IDR-1018 also influenced macrophage polarization to an unusual phenotype between that of classically activated (M1) and alternatively activated (M2) cells [7]. Beyond these immunomodulatory functions, IDR-1018 was found to be capable of eliminating biofilms of both Gram-positive and Gram-negative bacteria at concentrations far below its minimum inhibitory concentration against planktonic cells (<1 μg/mL ant-biofilm cf. >32 μg/mL antimicrobial activity) [5,8]. These immunomodulatory and antibiofilm properties of IDR-1018 have made it an attractive lead molecule to be further developed as a novel anti-infective to treat biofilm-associated infections as well as various inflammatory disorders.

In vivo studies with IDR-1018 have shown that the peptide can reduce inflammation-induced tissue damage in murine cerebral hypoxia–ischemia [9], cerebral malaria [10], and pulmonary tuberculosis [11] models. In murine models of *Staphylococcus aureus* orthopedic implant infections, IDR-1018 protected against failure of implants to osseointegrate and reduced overall inflammation [12]. IDR-1018 also promoted healing in porcine and murine *S. aureus*-infected wounds [13], as well as in various *in vitro* human wound models [14–16]. On its own, IDR-1018 has been used as an effective antimicrobial against *Pseudomonas aeruginosa* in a high-density murine cutaneous abscess model [17]. When used in conjunction with conventional antibiotics, IDR-1018 showed strong synergistic effects against cutaneous abscesses of different *ESKAPE* pathogens via interaction with the stringent response signaling molecule guanosine pentaphosphate (ppGpp) [17–19]. IDR-1018 further inhibits swarming motility of *P. aeruginosa*, a behavior that contributes to pathogen dissemination throughout the body [20,21].

Although there is a considerable amount of work around the mechanism and therapeutic potential of IDR-1018, little is known about its pharmacokinetics, or indeed that of any HDP. Bolouri *et al.* [9] conducted preliminary studies on the topic using a tritiated (^{3}H) version of IDR-1018. When injected intravenously (IV) as a 2 mg/kg bolus, ^{3}H-IDR-1018 was rapidly cleared from the blood with a distribution half-life of about 1 min. Blood levels soon plateaued at ~2 μg/mL until the end of the study at 4 h post-injection. Additionally, ^{3}H-IDR-1018 was found in high levels in the liver and spleen, both organs of the reticuloendothelial system (RES), at all time points and modest uptake into the brain was observed [9]. However, it should be noted that observations beyond 4 h and in organs other than the blood, brain, liver and spleen were not performed.

Less is known about the pharmacokinetics of extravascular IDR-1018, despite this being a commonly used route of administration for this peptide in various *in vivo* studies [9–13,17–20]. Haney *et al.* recently explored the behaviour of IDR-1018 when administered subcutaneously (SQ) into healthy mice [22]. The peptide precipitated upon subcutaneous injection in the skin and precipitates were visible to the naked eye at high doses when the injection site was excised [22]. The tendency for IDR-1018 to aggregate is largely due to the interactions with ions in solution and this phenomenon was found to follow the Hofmeister series of ions, with large anions having more of an influence overall [23]. Various formulations were assessed to prevent this aggregation tendency, with carboxylate-containing hyperbranched polyglycerol nanoparticles proving particularly effective [22,23]. Besides visual observation for signs of precipitation, no other pharmacokinetic-like assessments were made.

A lack of detailed pharmacokinetic data presents a hurdle in the clinical translation of IDR-1018 and other synthetic derivatives of natural HDPs [24]. Without knowing how a drug is adsorbed, distributed, metabolized and excreted, it is difficult to fully understand its mechanism, safety and efficacy profile. In this study, we set out to better define the pharmacokinetics of IDR-1018 in healthy mice using a gamma-emitting variant of the peptide together with nuclear tracing techniques. Single photon emission computed tomography coupled with X-ray computed tomography (SPECT/CT) was used to provide non-invasive and fully quantitative molecular data for the radiotracer labeled peptide along with detailed anatomical information. SPECT/CT scans were acquired at various IDR-1018 dose levels (2.5–13 mg/kg) using two different routes of administration (IV and SQ). Biodistributions were also performed where selected organs and tissues were removed and the radioactivity measured directly with a gamma counter. A concentration-dependent pharmacokinetic and toxicity profile was observed with the IDR-1018 radiotracer. Finally, histology was performed on selected organs to better understand the nature of the toxicity.

2. Results

2.1. Preparation and characterization of the IDR-1018 radiotracer

The radiotracer used in this study consists of the IDR-1018 peptide conjugated to the macrocyclic chelator 1,4,7-triazacyclononane-1,4,7-triacetic acid (NOTA), the latter of which can coordinate Gallium-67. Due to its relatively long half-life of 78.3 h, Ga-67 permits imaging over multiple days. The advantage of using NOTA-Ga for radiolabeling is that no harsh conditions, such as low pH or high temperatures are required. Also the resulting metal complex is neutral and has excellent *in vivo* stability (pM = 27.9) [25].

To prepare ^{67}Ga-NOTA-IDR-1018, an isothiocyanate derivative of NOTA was reacted with the N-terminus amine of IDR-1018 overnight in a mildly basic $NaHCO_3$ buffer [26]. The resulting thiourea linkage between the chelator and peptide has well-documented stability for downstream radiolabeling reactions and *in vivo* studies [26–29]. The crude reaction product was passed through a silica-gel cartridge, which captured NOTA-IDR-1018. Unreacted chelator was removed using water washes, and the modified IDR was eluted from the column using 0.01 M HCl (Fig. S1). Most of the peptide (62.7 ± 7.7%) eluted in the 2nd and 3rd acidic fractions, which were then pooled and used for downstream radiolabeling reactions. For the specific batch used to perform the *in vivo* work, 71.7% of the peptide was recovered in the aforementioned fractions. Radiolabeling was accomplished by incubating NOTA-IDR-1018 with ~25 MBq of $^{67}GaCl_3$ in 0.1 M HCl under mildly acidic conditions.

Radiochemical conversion (RCC), the fraction of the added ^{67}Ga that bound to NOTA-IDR-1018, was determined using instant thin-layer chromatography (ITLCs) [30]. In the ITLC system, the free radiometal Ga^{3+} forms a charged complex with ethylenediaminetetraacetic acid (EDTA) in the mobile phase and migrates to the top of the strip (Rf = 1), while the wanted radiometal bound to NOTA-IDR-1018 remains at the origin (Rf = 0), indicating excellent binding of the radioactive ^{67}Ga to the peptide (Fig. 1b). RCC was consistently ≥95% across multiple radiolabeling attempts, and specifically 98.5% for the batch used to perform the SPECT/CT imaging. The radiotracer was further characterized using sodium dodecyl sulfate polyacrylamide electrophoresis (SDS-PAGE) where we found that ^{67}Ga-NOTA-IDR-1018 migrated to a similar, yet slightly higher position than IDR-1018 in the gel (Fig. 1c). This slight shift is expected given that the ^{67}Ga-NOTA modification increased the molecular weight of the peptide from 1.5 kDa to 2.2 kDa. The peptide and radioactive signals from ^{67}Ga-NOTA-IDR-1018 co-localized to the same location in the gel, suggestive of an intact and stable radiotracer.

Due to the high RCC and inert composition of the labeling medium (dilute HCl in water), no further purification was performed on the radiotracer before moving *in vivo*. Instead, the pH and osmolality of the solution were adjusted with concentrated solutions of NaOH and NaCl, respectively, and combined with an appropriate amount of unmodified peptide to reach the desired dose level.

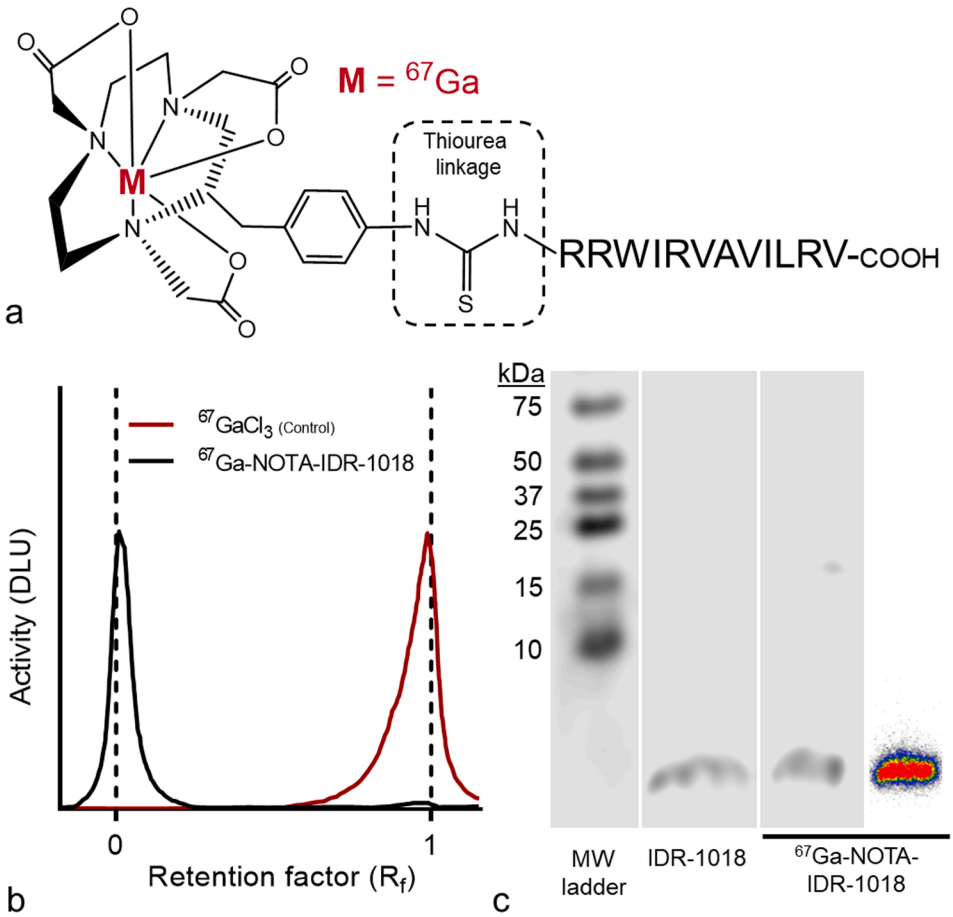

Fig. 1. Preparation of ^{67}Ga-NOTA-IDR-1018. (a) Structural overview of the IDR-1018-based radiotracer. (b) ITLC analysis of the radiolabeling reaction showed <1% of the radiometal was not bound to NOTA-IDR-1018, which is found almost entirely at Rf = 0 (black line). Free gallium-67 binds EDTA in the eluant and migrates to the top at $R_f = 1$ (red line; control). DLU: digital light units (c) SDS-PAGE analysis of ^{67}Ga-NOTA-IDR-1018. The radiolabelled and unmodified peptide showed a similar molecular weight. The peptide signal (greyscale; third lane) aligned with the radioactive signal (heatmap; fourth lane) in the gel. (For interpretation of the references to colour in this figure legend, the reader is referred to the web version of this article.)

2.2. Pharmacokinetics of low-dose intravenous and subcutaneous ^{67}Ga-NOTA-IDR-1018

Healthy mice (n = 3 per group) were injected with ^{67}Ga-NOTA-IDR-1018 as a 2.5 mg/kg IV bolus into the tail vein or a 3 mg/kg SQ injection into the dorsal surface. A series of SPECT/CT scans were then acquired for each mouse over a 48-h period. Imaging data is presented visually as representative top-view maximum-intensity projection (MIP) renderings over time of the fused SPECT and CT datasets. Quantitative time-activity curves of the SPECT dataset are provided for selected organs and tissues. Activity concentrations (AC) were reported as mean standardized uptake values (SUV_{mean}, g/mL), which was the average activity per unit volume within a particular site normalized to the injected radioactive dose and body weight of the animal [31]. Quantitative SPECT results are at times transformed into different units for clarity, such as percentage of the injected radioactive dose per organ (% ID/organ) or per gram (% ID/g), and the peptide concentration per unit volume (i.e., μg/g). Results for the *ex vivo* biodistribution performed on the animals following the final SPECT/CT scan are presented as % ID/organ and % ID/g.

After an IV bolus (2.5 mg/kg), a proportion of the dose was visible in the blood pool, namely the ventricles of the heart and carotid arteries, between 0.1 and 7 h post-injection (Fig. 2). Uptake into the lung tissue was also evident at early time points, along with elimination of ^{67}Ga-NOTA-IDR-1018 via the urine and feces. Pronounced uptake into the liver and spleen was observed in all scans. Accumulation of ^{67}Ga-NOTA-IDR-1018 into different regions of the skeleton, such as the vertebrae and certain joints, was evident after the 2 h scan.

Time-activity curves for the mice administered a low-dose IV bolus of ^{67}Ga-NOTA-IDR-1018 are shown in Fig. 3. ^{67}Ga-NOTA-IDR-1018 was found in the lung tissue at a concentration of 25.12 ± 2.58 μg/g (Activity Concentration [AC] = 2.89 ± 0.19 g/mL; 48.10 ± 4.37% of the initial dose [ID]/g) at 0.1 h post-injection (Fig. 3a); just over 8% of the injected dose was within the lungs at this time. The blood contained 23.22% of the injected dose at 0.1 h post-injection, with an concentration of 9.09 ± 1.43 μg/mL (AC = 4.02 ± 0.53 g/mL; 16.47 ± 2.49% ID/g. Concentrations of ^{67}Ga-NOTA-IDR-1018 in the blood fell rapidly after injection, with a distribution-phase half-life ($t_{1/2\alpha}$) of just under 0.1 h. Between 2 and 7 h post-injection, however, blood concentrations of the radiotracer were largely sustained at ~4 μg/mL (AC = ~2 g/mL; ~8% ID/g). The area under the curve ($AUC_{0\text{-}\infty}$) was 83.15 ± 2.71 μg/(mL•h) and the mean residence time ($MRT_{0\text{-}\infty}$) was 10.23 ± 1.94 h.

A whole-body time-activity analysis found that the elimination of low-dose IV ^{67}Ga-NOTA-IDR-1018 from mice followed two-phase decay kinetics (i.e., the sum of a slow and fast decay process). The half-life of the fast decay process was 2.6 h while the slow half-life was 155 h. At 48 h post-injection, only 58.13 ± 2.59% of the injected dose remained (Fig. 3f).

Low-dose IV ^{67}Ga-NOTA-IDR-1018 was cleared from the blood hepatically, splenically and renally (Fig. 3b and 3c). Activity concentrations in the liver were 2.49 ± 0.52 g/mL a few minutes following administration, peaked at 2 h post-injection at 10.74 ± 0.93 μg/g (AC = 5.05 ± 0.44 g/mL; 20.58 ± 1.78% ID/g), and gradually decreased thereafter. The liver contained 23.13 ± 2.42% of the injected dose at its peak, and only ~10% of the injected dose at the initial and final scans. The distribution of ^{67}Ga-NOTA-IDR-1018 into the spleen followed a similar pattern to that of the liver; activity concentrations peaked at 2 h post-injection at 10.45 ± 1.27 μg/g (AC = 4.93 ± 0.82 g/mL; 20.04 ± 2.66% ID/g), gradually decreasing to just over 3 g/mL by the end of the study. The proportion of the dose in the spleen was quite small with only ~1% of the injected dose at all time points. Renal clearance was evident by the presence of ^{67}Ga-NOTA-IDR-1018 in both the kidneys and urine. Activity concentrations in both sites peaked at 0.1 h post injection, with

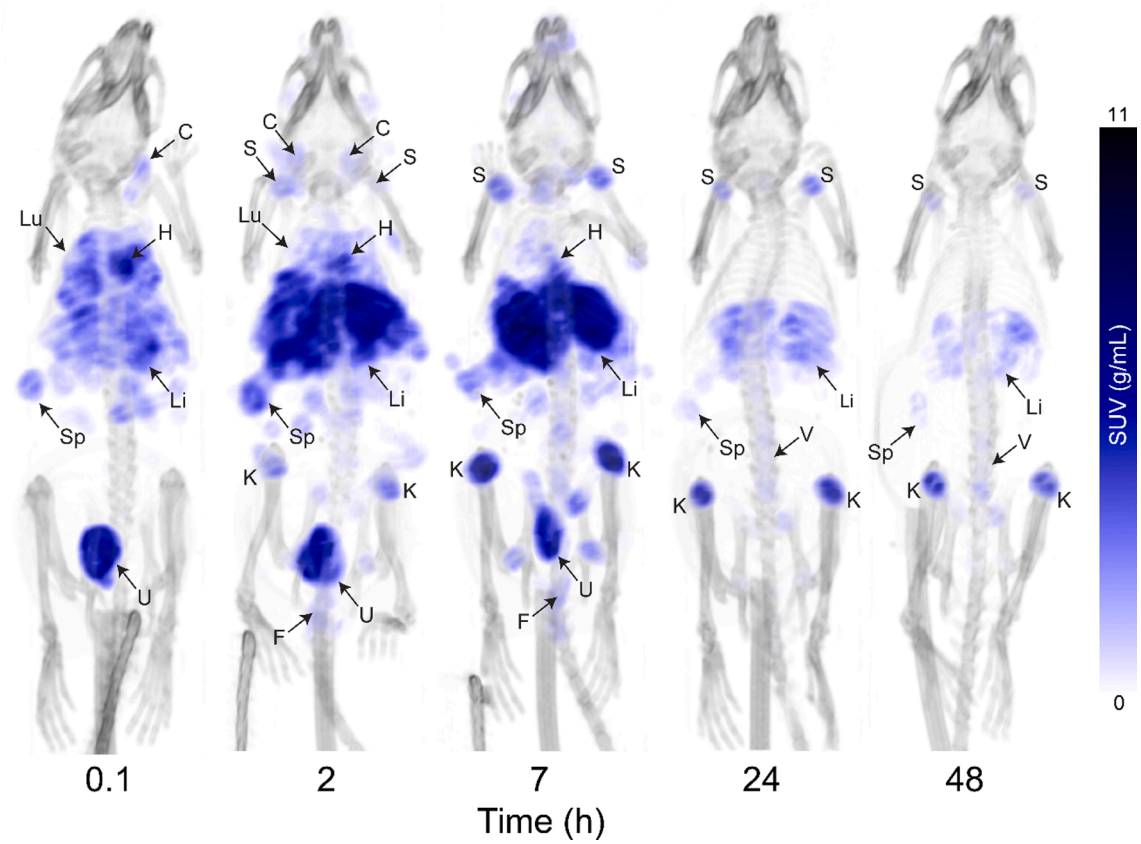

Fig. 2. Representative SPECT/CT renderings of IV ^{67}Ga-NOTA-IDR-1018 at 2.5 mg/kg. Renderings are shown from a single animal over a 48-h period. ^{67}Ga-NOTA-IDR-1018 was observed in the blood, lung tissue and excretory pathways in early scans. Prominent uptake was also evident in the liver, spleen and certain regions of the skeletal system over time. SPECT in blue tones, CT in greyscale. C, carotid artery; F, feces; H, heart (blood pool); K, knee region; Li, liver; Lu, lung; S, shoulder region; Sp, spleen; U, urine; V, vertebrae. (For interpretation of the references to colour in this figure legend, the reader is referred to the web version of this article.)

5.76 ± 0.59 μg/g (AC = 2.69 ± 0.35 g/mL; 11.05 ± 1.22% ID/g) in the kidney and 12.13 ± 1.88 μg/mL (AC = 5.36 ± 0.60 g/mL;22.53 ± 3.21% ID/g) in the urine. The urine contained between 1% and 2.5% of the injected dose up to the 7 h post-injection scan, deceasing substantially thereafter.

The distribution profile of ^{67}Ga-NOTA-IDR-1018 into the skeletal system, when administered as a 2.5 mg/kg IV bolus, was rather variable (Fig. 3d). Prominent uptake was observed in the knee and shoulder, regions composed of a complex mixture of cartilage, ligaments/ tendons, and the epiphyseal aspects of long bones. Uptake into the knee region peaked at 7 h post-injection at 4.87 ± 0.49 g/mL. Peptide concentrations within the knee ranged between 6 and 8 μg/g from 2 to 48 h post-injection. The distribution of ^{67}Ga-NOTA-IDR-1018 to the shoulder region closely mirrored that of the knee, albeit at slightly lower concentration. Uptake of ^{67}Ga-NOTA-IDR-1018 into the diaphysis of a long bone (shaft of the femur) and vertebrae peaked later at 24 h post-injection with ACs of 0.83 ± 0.41 and 2.38 ± 0.35 g/mL at 0.1 and 24 hr, respectively.

^{67}Ga-NOTA-IDR-1018 poorly distributed to the brain as a low-dose IV bolus, with a concentration of 0.61 ± 0.17 μg/g (AC = 0.28 ± 0.081 g/mL;1.16 ± 0.33% ID/g) at 0.1 h post injection (Fig. 3e). Approximately 0.5% of the injected dose was found in the brain at the first scan but remained <0.1% ID/organ for the remainder of the study.

Representative SPECT/CT renderings for the SQ ^{67}Ga-NOTA-IDR-1018 group are shown in Fig. 4. Notably, only the injection site is readily visible at all time points over the course of the experiment. Quantitative image analysis of the injection site (Fig. 5) found that ^{67}Ga-NOTA-IDR-1018 was rapidly absorbed from the SQ tissue and followed two-phase exponential decay kinetics — a fast half-life of 1.8 h and a slow half-life of 50 h. This might be due fast drainage of most of the radiolabeled peptide into the vascular system, with just a small percentage interacting with some local cells and/or proteins. After interaction, the peptide left the injection site much slower, with the slow half-life. Only ~5% of the injected dose remained at the injection site at 48 h. The average concentration of ^{67}Ga-NOTA-IDR-1018 at the injection site was 241.03 ± 56.08 μg/g (AC = 73.10 ± 17.90 g/mL;356.11 ± 89.19% ID/g) shortly after injection. The tissue concentration of ^{67}Ga-NOTA-IDR-1018 within the hottest voxel in the injection site at 0.1 h was 4.97 ± 1.55 mg/g. Activity concentrations at the site of injection were relatively stable between 4 and 48 h post-injection at around 50 μg/g (AC = ~15 g/mL; ~75% ID/g). The size of the injection site remained rather steady between 0.1 and 4 h post-injection (~0.3 mL) but decreased to a quarter of its original size by 48 h post-injection.

Quantitative analysis of the SQ ^{67}Ga-NOTA-IDR-1018 SPECT dataset (Fig. 6) revealed modest uptake of the radiotracer into various organs besides the injection site, although this was difficult to visualize from the SPECT/CT renderings. Concentrations of ^{67}Ga-NOTA-IDR-1018 were negligible at all assessed sites at 0.1 h post-injection. Peak concentrations at most sites were achieved at 4 h post-injection, which was in line with the fast initial phase of absorption of ^{67}Ga-NOTA-IDR-1018 from the injection site. At the 4 h scan, a maximum blood concentration of 0.90 μg/mL (AC = 1.27 ± 0.27 g/mL; 5.39 ± 1.09% ID/g) was observed, indicating approximately 7% of the injected dose was within the blood pool (Fig. 6a). Pharmacokinetic modeling of the blood data revealed that the $AUC_{0\text{-}\infty}$ was 80.82 ± 15.18 μg/(mL•h) and the $MRT_{0\text{-}\infty}$ was 17.94 ± 2.69 h. Lung uptake was far less pronounced than observed with IV ^{67}Ga-

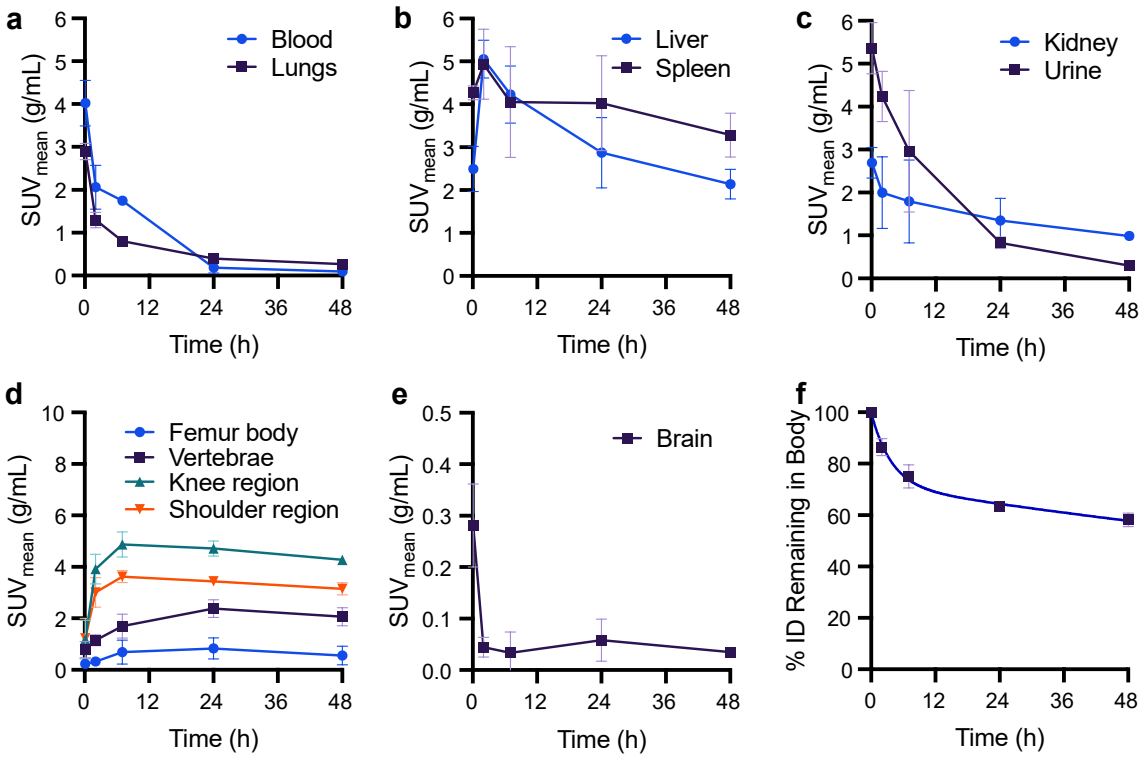

Fig. 3. Time-activity curves for the 2.5 mg/kg IV ^{67}Ga-NOTA-IDR-1018 SPECT dataset.(a–d) Analysis for select organ systems, in units of SUV_{mean}. Temporary lung uptake was observed at early scan times, along with sustained blood concentrations of ^{67}Ga-NOTA-IDR-1018. Uptake of the radiotracer by the liver and spleen, along with renal clearance of the peptide was also evident. ^{67}Ga-NOTA-IDR-1018 gradually accumulated in bony tissues, and poorly distributed to the brain. (f) Whole animal analysis, fit with two-phase decay kinetics. Approximately 40% of the injected dose had been eliminated by the time of sacrifice. Some error bars may not be visible behind plot symbols. n = 3 animals.

NOTA-IDR-1018; concentrations of the radiotracer were negligible at 0.1 and 48 h post-injection but remained around 3.5 μg/g (AC = ~0.3 g/mL; ~5% ID/g) between 4 and 21 h (Fig. 6a). Maximum uptake of ^{67}Ga-NOTA-IDR-1018 into the liver and spleen occurred at 21 h post-injection at 2.94 ± 0.37 μg/g (AC = 1.02 ± 0.13 g/mL; 4.33 ± 0.58% ID/g) and 2.21 ± 0.48 μg/g (AC = 0.77 ± 0.18 g/mL; 3.28 ± 0.81% ID/g), respectively (Fig. 6b). Approximately 5% of the injected dose was within the liver tissue at its peak, decreasing to just under 4% ID at the end of the study. The spleen contained only ~0.1% of the injected dose between 4 and 48 h post-injection. The activity concentration in the kidneys remained at around 2.5 μg/g (AC = ~1 g/mL; ~4% ID/g) from the 4 h scan onward (Fig. 6c). Peak urine concentrations of ^{67}Ga-NOTA-IDR-1018 were also observed at 4 h post-injection at 2.22 ± 0.16 g/mL; the peptide concentration at this time was approximately 7 μg/mL and comprised about 2.5% of the injected dose. The AC within the skeletal system largely peaked at 21 h post-injection at ~0.8 g/mL in the diaphysis of the femur, ~2.8 g/mL in the vertebrae and between 3 and 3.5 g/mL in the knee and shoulder regions (Fig. 6d). Activity levels in the brain were always <0.25 g/mL (Fig. 6e). Whole-body analysis found that ^{67}Ga-NOTA-IDR-1018 was eliminated from the body following 2 phase decay kinetics with a fast initial half-life of 1.5 h followed by a slow half-life of 88.6 h (Fig. 6f). Only approximately 50% of the injected dose remained in the animals at the end of the SPECT/CT imaging series.

Results from the biodistribution, assessed *ex vivo*, at 48 h post-injection are shown in Fig. 7 and Table S1 for both the SQ and IV groups. Putting aside a slight difference in the dose administered to each of the groups (2.5 vs. 3 mg/kg), a similar distribution pattern was observed upon dissection for both routes of administration. The bones in both groups contained ~10% of the injected dose (tissue concentration of ^{67}Ga-NOTA-IDR-1018 ~6% of the injected dose/g). The muscle of the IV and SQ groups contained approximately 3% of the injected dose despite a relatively low tissue concentration of around 0.3% of the injected dose/g. Only a small amount of ^{67}Ga-NOTA-IDR-1018 remained in the blood for both injection routes (~0.4% ID/g, ~0.5%/organ). After removing the blood, the heart tissue contained a small residual concentration of ^{67}Ga-NOTA-IDR-1018 at 0.5% ID/g. However, the heart along with the brain and lymph nodes contained a negligible proportion of the injected dose. The concentration of radiotracer in the lymph nodes was elevated compared to most tissues at 5.18 ± 1.05% ID/g for the SQ group and 2.35 ± 2.37% ID/g for the IV group. There was a trend, although not statistically significant, for higher lymphatic uptake in the SQ group, potentially because this measurement used the inguinal lymph nodes that (partly) drained the SQ injection site. A similar degree of uptake was observed in the kidneys at ~4% ID/g and ~1.3% ID/organ for both routes of administration. There was a trend towards a higher activity concentration of ^{67}Ga-NOTA-IDR-1018 in the urine of the SQ animals (2.31 ± 0.38 vs. 1.39 ± 0.48% ID/g, likely due to ongoing absorption (and then renal clearance) of the remaining dose from the injection site. Approximately 3% ID/g was observed in the feces in both groups, along with similar amounts and concentrations of ^{67}Ga-NOTA-IDR-1018 in the organs of the gastrointestinal tract after the luminal contents were removed.

Despite the above similarities in the *ex vivo* biodistribution, there were a couple of organs where the distribution of ^{67}Ga-NOTA-IDR-1018 differed significantly. The liver of the 2.5 mg/kg IV bolus animals contained a much higher proportion of the total injected dose (10.10 ± 0.68% vs. 4.31 ± 0.26% of the injected dose/organ) and a higher activity concentration (8.99 ± 0.41% vs. 3.66 ± 0.42% of the injected dose/g) than the 3 mg/kg SQ group. The same was observed in the spleen, with 14.22 ± 1.49% ID/g and 0.77 ± 0.10%/organ for the IV bolus group and 2.60 ± 0.20% ID/g and 0.14 ± 0.014%/organ for the SQ group.

The biodistribution values closely matched those calculated from the final SPECT/CT scan acquired at about the same time, adding an

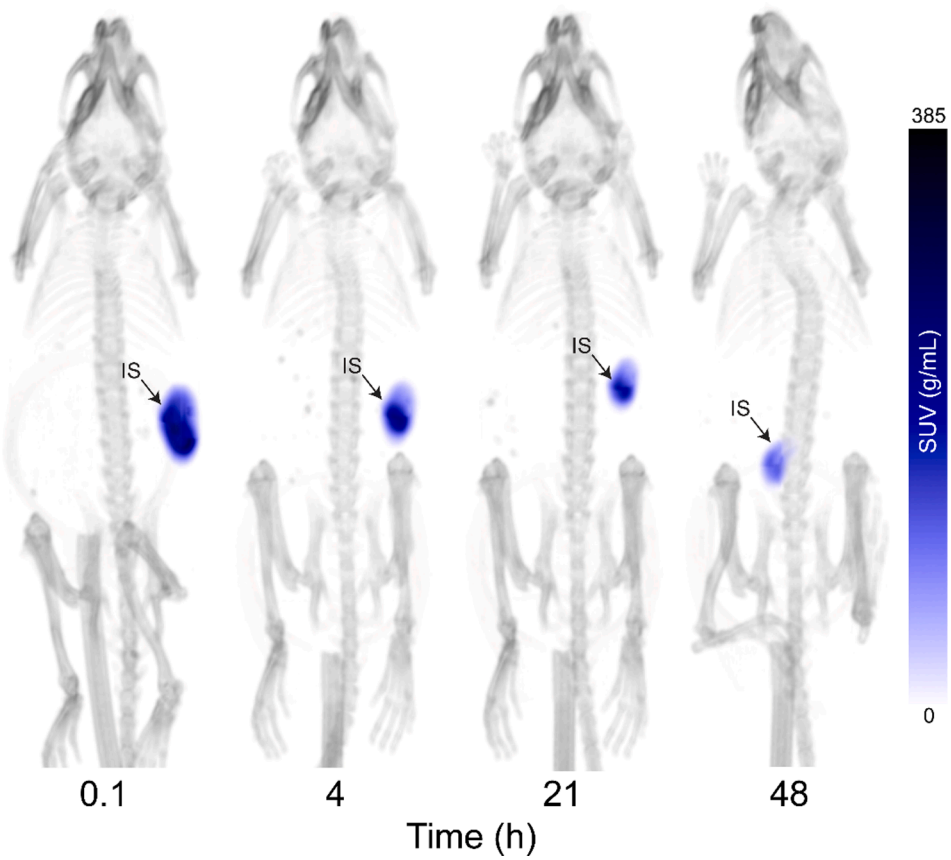

Fig. 4. SPECT/CT renderings of 3 mg/kg SQ ^{67}Ga-NOTA-IDR-1018. Representative renderings are shown from a single animal over a 48-h period. Only the injection site (IS) is visible due to the high concentration of ^{67}Ga-NOTA-IDR-1018 at that site in relation to other organs/ tissues. SPECT in blue tones, CT in greyscale. NB: the injection site appears to move, but this was due to the position of the mouse between SPECT/CT scans and the tape used to secure the animals, which stretched the skin in the holder. (For interpretation of the references to colour in this figure legend, the reader is referred to the web version of this article.)

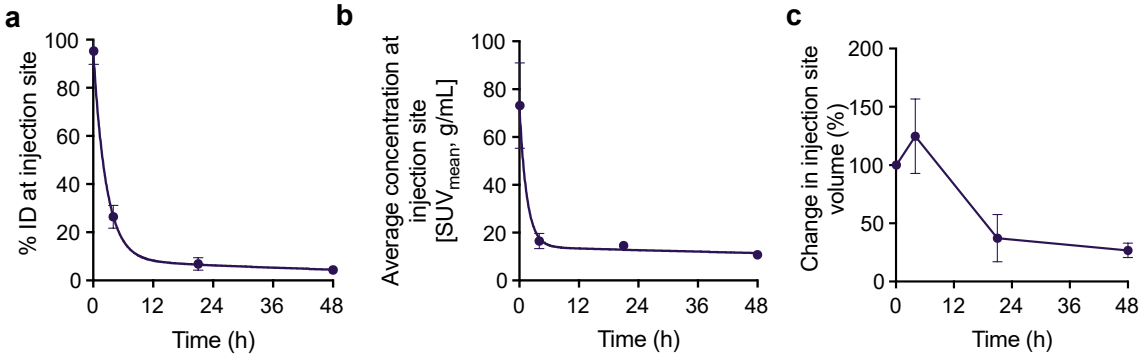

Fig. 5. Quantitative analysis of the 3 mg/kg SQ ^{67}Ga-NOTA-IDR-1018 injection site. (a) Percentage of the injected dose remaining at the site of injection over time, fit using a 2-phase exponential decay kinetics. (b) Average concentration of ^{67}Ga-NOTA-IDR-1018 at the site of injection, in units of SUV_{mean} and fit using a 2-phase exponential decay kinetics. (c) Change in the volume of the injection site over time. The proportion of the injected dose and concentration of radiotracer fell rapidly during the first few hours at the site of injection, and largely plateaued from the 4 h timepoint onward. Some error bars may not be visible behind plot symbols. n = 3.

additional degree of confidence in the results obtained in this study.

2.3. Pharmacokinetics of high-dose intravenous ^{67}Ga-NOTA-IDR-1018

Healthy mice were administered IV boluses of ^{67}Ga-NOTA-IDR-1018 at 7 and 13 mg/kg (n = 1/ group) and imaged with SPECT/CT to determine if the dose level influenced the pharmacokinetics of the peptide.

Compared to the 2.5 mg/kg IV group discussed above, higher doses of ^{67}Ga-NOTA-IDR-1018 were poorly tolerated. The animal administered the 7 mg/kg dose died within ~5 min of injection while on the SPECT/CT scanner. The 13 mg/kg dose caused death very quickly, within seconds, and the mouse was subsequently scanned after its decease. In both cases, the mice exhibited signs of severe respiratory distress (i.e., labored breathing/gasping) and appear to have died from respiratory arrest.

Representative SPECT MIP renderings and quantification of high-dose IV ^{67}Ga-NOTA-IDR-1018 within select organs are shown in Fig. 8. Imaging data helps to explain the above clinical observations since there was an appreciable increase in ^{67}Ga-NOTA-IDR-1018 within the lung tissue as a function of dose. More specifically, the activity concentration in the lungs increased from approximately 3 g/mL at the 2.5 mg/kg dose level to ~10 g/mL (~170% ID/g) at both the 7 and 13 mg/kg dose levels. This meant that approximately 25% of the injected

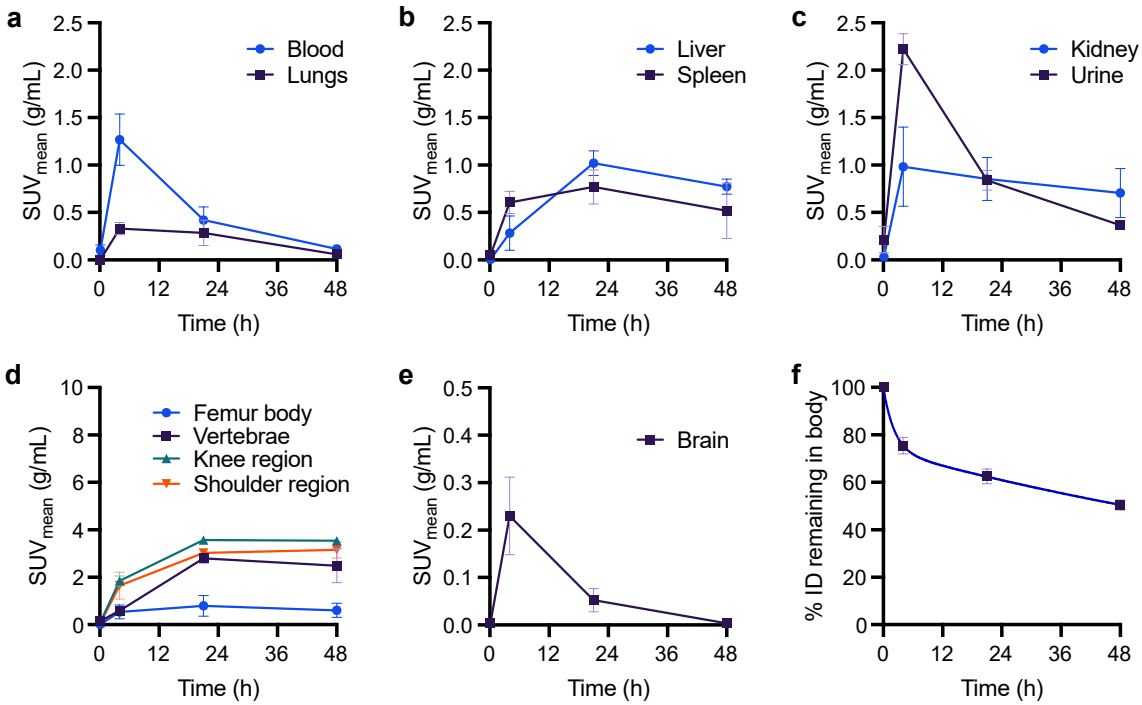

Fig. 6. Time-activity curves for the 3 mg/kg SQ ^{67}Ga-NOTA-IDR-1018 SPECT dataset. (a–e) Analysis for select organ systems, in units of SUV_{mean}. Concentrations of ^{67}Ga-NOTA-IDR-1018 within most sites, such as the blood, lungs, kidney, urine and brain, peaked at 4 h post-injection. Accumulation of ^{67}Ga-NOTA-IDR-1018 in other organs, such as the liver, spleen and skeletal system was more delayed, peaking at 21 h post-injection. (f) Whole animal analysis, fitted to two-phase decay kinetics. Some error bars may not be visible behind plot symbols. n = 3.

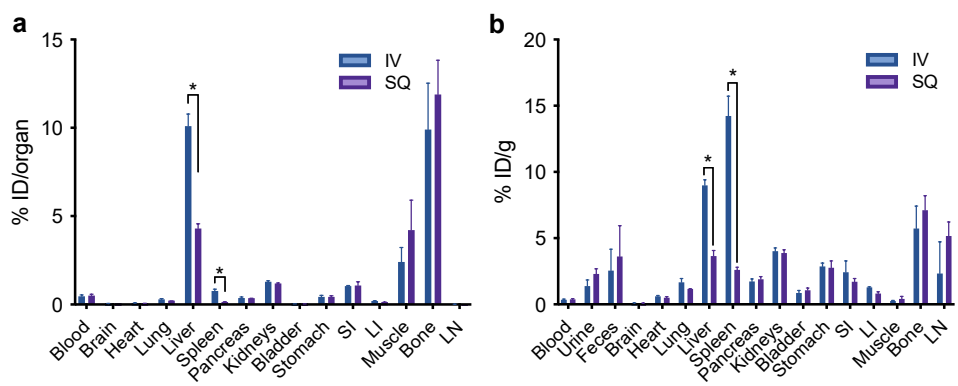

Fig. 7. Biodistribution of IV (2.5 mg/kg) and SQ (3 mg/kg) ^{67}Ga-NOTA-LL-37 at 48 h post-injection as (a) % ID/organ and (b) % ID/g. The majority of activity was found within the liver, bone and muscle of both groups. High tissue concentrations were evident in the spleen, liver, bone and lymph nodes. LI, large intestine; LN, lymph node; SI, small intestine. *p < 0.05. n = 3/ group.

dose was found within the lung tissue at 7 and 13 mg/kg. Tissue concentrations of the peptide reached 294.9 μg/g at 7 mg/kg and 522.9 μg/g at 13 mg/kg. Activity concentrations within the liver were around 2.5 g/mL (10% of the injected dose/g) regardless of the dose level, resulting in peptide concentrations of 16.6 μg/g at 7 mg/kg and 35.7 μg/g at 13 mg/kg. Approximately 10% of the injected dose had distributed to the liver of the high-dose IV ^{67}Ga-NOTA-IDR-1018 mice within the few minutes they survived post-injection. The concentration of ^{67}Ga-NOTA-IDR-1018 within the blood decreased as the dose of the radiotracer was escalated, from 1.81 g/mL (7.54% of the injected dose/g) at 7 mg/kg to 1.13 g/mL (4.70% of the injected dose/g) at 13 mg/kg. A peptide concentration of ~15 μg/mL was achieved in the blood for both the 7 and 13 mg/kg dose levels. Renal clearance of ^{67}Ga-NOTA-IDR-1018 also decreased upon dose escalation. Kidney concentrations of ^{67}Ga-NOTA-IDR-1018 fell from 2.69 ± 0.35 g/mL at 2.5 mg/kg to 1.73 g/mL at 13 mg/kg. Urine concentrations of the radiotracer followed accordingly, dropping from just over 5 g/mL at 2.5 mg/kg to 0.10 g/mL at 13 mg/kg. Quite low levels of activity (<1 g/mL) were observed in the brain, spleen and skeleton (femur body, vertebrae, knee/ shoulder regions).

2.4. Toxicity of high-dose intravenous IDR-1018

To further explore the respiratory toxicity described above, mice were injected with an IV bolus 8 mg/kg (n = 2) and 15 mg/kg (n = 2) IDR-1018. Unmodified peptide was used here to ensure that the toxicity observed was not due to the addition of the ^{67}Ga-NOTA moiety. Upon injection, similar clinical signs were observed as with the radiotracer. The mice injected with the highest dose of IDR-1018 stopped breathing and died within seconds of injection. The 8 mg/kg animals breathing became labored immediately following injection, and the animals died within a couple of minutes. The lungs were then removed for histological examination after paraffin embedding and staining with

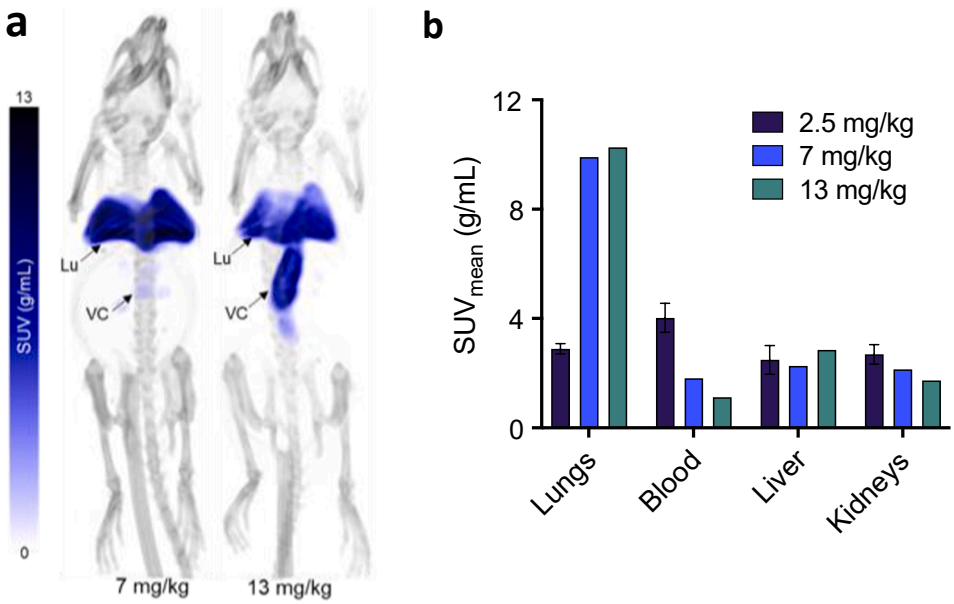

Fig. 8. SPECT/CT renderings (a) and quantitative analysis (b) of high-dose IV ^{67}Ga-NOTA-IDR-1018. Upon dose-escalation, IV ^{67}Ga-NOTA-IDR-1018 accumulated to a greater extent in the lung tissue (Lu), and uptake was less pronounced in most other organs. A portion of the dose could be found in the vena cava (VC), particularly at the 13 mg/kg dose level; damage to the lung or stoppage of the heart due to ^{67}Ga-NOTA-IDR-1018 may have prevented a portion of the dose from progressing beyond this point. SPECT in blue tones, CT in greyscale. (For interpretation of the references to colour in this figure legend, the reader is referred to the web version of this article.)

hematoxylin and eosin (Fig. 9). There were no signs of the peptide precipitating and embolizing or becoming mechanically trapped within the lung vasculature. Instead, there was diffuse congestion of the pulmonary vascularity, including the capillary beds, with a distinct pattern of distention of the medium sized pulmonary veins. Occasional focal to locally extensive areas of alveolar hemorrhage were present, and in these areas, there was leakage of serum into the alveoli. There was a mild, diffuse mononuclear cell region throughout the alveolar septae with occasional neutrophils also being present (Fig. S2). The heart appeared to be histologically normal at both the 8 and 15 mg/kg dose levels (Fig. S3). Significant hemolysis was visually observed in blood samples from the mice that received high doses of IV IDR-1018 compared to the saline controls.

To further explore the mechanism of the toxicity observed to the lung vasculature and parenchyma, IDR-1018 was added to cultured endothelial cells (HUVEC cells) *in vitro*. Phase contrast micrographs were acquired over a 24 h period using a live-cell imaging platform (Fig. S4). At very high concentrations (300 μg/mL), similar to the lung tissue concentrations observed in the 7 mg/kg IV ^{67}Ga-NOTA-IDR-1018 SPECT, the HUVEC cells were essentially dissolved within a few minutes of incubation with the peptide. At lower concentrations (37.5 μg/mL), more in-line with the lung concentrations observed at the 2.5 mg/kg IV ^{67}Ga-NOTA-IDR-1018 dose level, the cells were intact at 0.1 h. With time, the cells treated with 37.5 μg/mL IDR-1018 started to show morphological signs of toxicity [32] (i.e., blebbing, changes in the cell size/ shape, etc.). Small precipitates/particles of the drug could also be observed at various dose levels. These particles formed rapidly when added to the cells and they were present at the first timepoint just a few minutes after adding the peptide. The particles persisted and did not appear to re-dissolve back into solution with time.

3. Discussion

Using the long-lived gamma-emitting isotope gallium-67, we developed a novel radiotracer for IDR-1018. The labelled ^{67}Ga-NOTA-IDR-1018 peptide was stable, did not degrade or crosslink during the radiolabeling process, and was of high enough radiochemical purity to allow pharmacokinetic studies in mice in real time. The distribution of ^{67}Ga-NOTA-IDR-1018 in healthy mice was significantly different from that of free gallium-67 and the ^{67}Ga-NOTA chelate, adding confidence that the radiotracer *in vivo* demonstrated radiochemical stability. Free gallium-67, following IV injection, is taken up by the iron transport protein transferrin [33–35]. Over time, gallium-67 is taken up by tissues that express the transferrin receptor (i.e., liver) or through affinity for

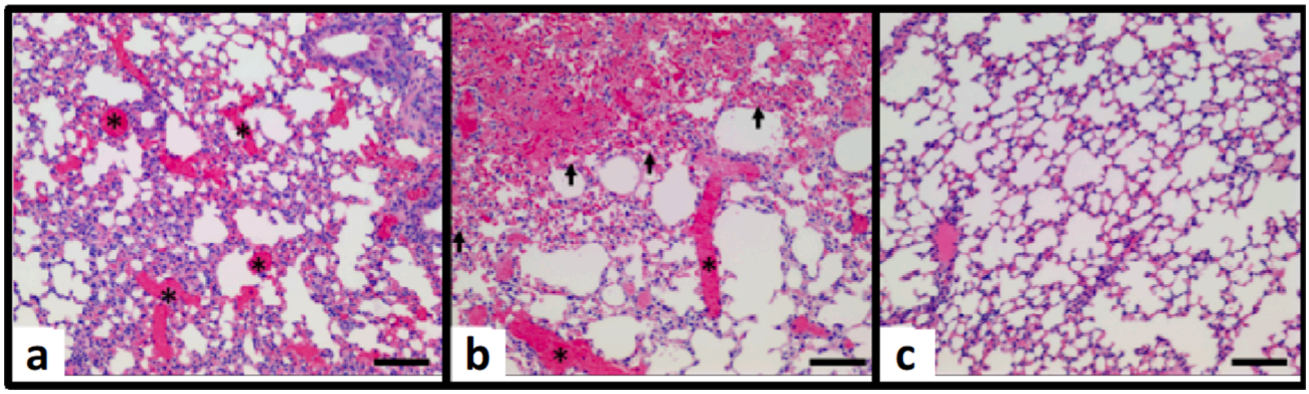

Fig. 9. Representative 100X micrographs of the lungs of mice treated with high-dose IV IDR-1018. At 8 mg/kg (a), general congestion of the tissue, less extensive alveolar hemorrhage and dilation of the medium sized veins were observed. At 15 mg/kg (b), areas of severe alveolar hemorrhage (arrow heads) and dilation of the medium-sized pulmonary veins (stars) were visible. Micrographs of saline-treated mice (c) are shown as controls. Scale bars are 100 μm.

hydroxyapatite, which accumulates in the osseus aspects of the bones [33–35]. On the other hand, the ^{67}Ga-NOTA is cleared rapidly following an IV injection via the kidneys, and accumulates poorly in any tissue [35,36].

When injected as a 2.5 mg/kg IV bolus, ^{67}Ga-NOTA-IDR-1018 was rapidly cleared from the central compartment with a $t_{1/2\alpha}$ of ~5 min. The activity concentration and amount of radiotracer in the blood was only ~9 μg/mL, which was ~23% of the injected dose at 0.1 h post-injection. Interestingly, a plateau of ^{67}Ga-NOTA-IDR-1018 was observed in the blood for the next few hours at around ~4 μg/mL, ~10% of the injected dose. Bolouri *et al.* [9] observed a similar distribution profile in the blood with ^{3}H-IDR-1018, albeit at slightly lower concentrations due to a lower injected dose of 2 mg/kg. ^{3}H-IDR-1018 had a $t_{1/2\alpha}$ of ~1 min, and the highest reported blood concentration was ~8 μg/mL at 2 min post-injection. Approximately 20% of the injected dose was present in the blood at this time. Blood concentrations then decreased and remained around 3 μg/mL, ~10% of the injected dose from 0.25 h to the end of the study at 4 h post-injection.

Rapid clearance from the blood after IV bolus injection is a relatively well-established concept for most HDPs when administered parenterally [37–39]. Thus analogous rapid clearance (or low levels shortly after injection) was observed for ^{67}Ga-labeled LL-37 [35], ^{68}Ga-DOTA-D-Tyr-danalexin [40], ^{64}Cu-DOTA-HLys [41], ^{125}I-caerin1.9 [42], ^{99m}Tc-labeled melittin [43], tritiated RTbtR [44], and ^{124}I-labeled SET-M33L [45]. Similarly, the slower second phase of elimination was observed for S016-1271 [46] and NAB7061/NAB739 [47] that rapidly distributed from the blood, but had a more delayed elimination phase half-life ($t_{1/2\beta}$) of 42 and 68 min, respectively. Similar elimination kinetics were observed for ^{99m}Tc-labeled lactoferrin 1–11 [48], human neutrophil peptide-1 [49], ubiquicidin 29–41 [50,51] ($t_{1/2\beta}$s of 30–175 min in mice) as well as tritiated HDP [52], Thanatin [53], Rhesus theta defensin 1 [54], and Onc72 [55]. AUC and MRT values of other HDPs were generally less than ^{67}Ga-NOTA-IDR-1018 (AUC: 83 μg/(mL•h); MRT: 10 h) since most other peptides lacked a plateau-phase in the blood that increased systemic exposure. Examples include ^{67}Ga-NOTA-LL-37 (AUC: 28 μg/(mL•h):, MRT: 11 h) [35], Onc72 (AUC: 0.8 μg/(mL•h):, MRT: 0.3 h) [55] and S016-1271 (AUC: 32 μg/(mL•h), MRT: 1.3 h) [46].

The plateauing blood levels of ^{3}H-IDR-1018/^{67}Ga-NOTA-IDR-1018 within the first few hours post-injection is quite unusual for a small peptide-based drug, although other HDPs, particularly Onc112, have exhibited related behavior. Following a 5 mg/kg IV bolus to mice, an initial blood concentration of Onc112 at 4 μg/mL was reported at 5 min post-injection, which increased to 5.4 μg/mL between 10 and 20 min, and then decreased rapidly [55]. Many factors may be at play here, but it has been postulated that a local depot of HDP is formed within the vein into which the peptide is injected, and this is then released back into the circulation over time [55]. This depot has been proposed to form due to the tendency of HDPs to interact with cell membranes and the high local concentrations of HDP within the vasculature following a bolus dose that promotes such interactions [55]. In contrast, imaging here with ^{67}Ga-NOTA-IDR-1018 however suggests that this 'HDP reservoir' is not in the lining of the injected vein, but instead in the lungs. The lungs contain the first capillary bed following an IV injection, and have an extensive membrane surface area (124 cm^2 in mice) for HDP interaction [56]. High levels of lung uptake were similarly observed with other HPDs shortly after injection, such as PEGylated ^{124}I-SET-M33l with initial lung concentrations exceeded exceeding 100% ID/g, which decreased to ~25% ID/g at 30 min-post-injection and negligible levels by 6 h PI [45]. However, significant and temporary lung uptake is not universal amongst HDPs and has not been observed for many other compounds [41,42,44,49,52,57]. There may of course be other factors prolonging the circulation half-life of select HDPs like IDR-1018 and Onc112, such as a propensity of HDPs to bind to plasma proteins that circulate well such as albumin [58] and apolipoprotein A-1 [59].

In this study, we observed a dose-dependent uptake of ^{67}Ga-NOTA-IDR-1018 into the lungs. Activity concentrations at this site increased from ~3% ID/organ following a 2.5 mg/kg IV bolus to ~10% ID/organ at 7–13 mg/kg. A marked increase in the damage to the lung tissue was observed at the higher doses. These observations can be explained by the concentration-dependent manner in which IDR-1018 interacts with cell membranes. IDR-1018 does not cause significant membrane perturbations at the concentrations required to generate a therapeutic effect (<100 μg/mL) [5]. Instead of directly lysing bacterial cells, IDR-1018 translocates across their membranes to interact with intracellular targets, such as ppGpp [5,8]. IDR-1018 acts similarly to exert its effects on immune cells [5,60–62]. Much higher concentrations (>375 μg/mL) are required to disrupt membranes, cause a significant degree of hemolysis [5] and as observed in this study it required ≥150 μg/mL to lyse HUVEC cells. Other HDPs, such as LL-37, disrupt membranes and cause toxicity at lower concentrations (25–50 μg/mL) when compared to IDR-1018 [63–65]. Interestingly, we observed much higher levels of ^{67}Ga-NOTA-LL-37 in the lung at 0.1 h post-injection cf. ^{67}Ga-NOTA-IDR-1018 [35].

Although HDPs are rapidly cleared from the blood, there is not so much agreement on their specific means of clearance. Thus ^{67}Ga-NOTA-LL-37 was predominately cleared hepatically over a 48 h period (40–70% of the injected dose), with high AC also observed in the spleen (5–6 g/mL) [35] and less prominent renal clearance. In contrast, ^{67}Ga-DOTA-D-Tyr-danalexin was predominately cleared renally [40]. Other peptides demonstrated preferential accumulation in one or more of the liver, spleen, kidneys, lymph nodes and/or urine [41–45,47–52,66,67].

The mechanism of clearance of IDR-1018 from the blood may be the result of various factors. Soman *et al.* [43] hypothesized that HDPs insert into RBC membranes upon injection into the blood, and the lysed cells and debris are then cleared away by filtration organs like the liver and spleen. Hemolysis has been reported before for IDR-1018 [5] but not in whole blood although it was observed in this study at high dose levels. It is also well-established that IDR-1018 has a strong propensity to precipitate/aggregate in the presence of salt and in biological media due to the Hofmeister effect [23]. Precipitation was observed in this study around HUVEC cells treated with the peptide. As with lysed cells, debris and particulates are efficiently removed from the blood by phagocytic cells that reside within the reticuloendothelial system organs of the liver, spleen and bone marrow [68–70]. Besides reticuloendothelial system uptake, a portion of ^{67}Ga-NOTA-IDR-1018 was cleared renally. The peptide is below the MW cut-off for the glomerulus (30–50 kDa) [71], and if very fine particulates are formed in the blood (<5 nm) [72], those could also be removed by the kidney.

Furthermore, Bolouri *et al.* [9] observed that ^{3}H-IDR-1018 accumulated in the brain tissue over time, increasing from 0.3 μg/g at 2 min post-injection to 1.5 μg/g at 4 h. We observed an intital concentration in the brain at 0.1 h post-injection of 0.6 μg/g, and concentrations of <0.1 μg/g for the remainder of the study. Crossing the blood brain barrier (BBB) is favored by lipophilic compounds (log(P) 2–5) with a molecular weight <0.5 kDa, amongst other properties [73]. IDR-1018 is well outside of these parameters with a MW of ~1.5 kDa and a net positive charge of +5, although its amphiphilicity means it might be able to permeate the BBB. The added MW from the ^{67}Ga-NOTA moiety (0.5 kDa) may have hindered IDR-1018 uptake into the brain when compared to that observed with the ^{3}H-labeled molecule. Furthermore, very low concentrations in the brain (~0.001 μg/g) were reported for ^{125}I-labeled proline-rich HDPs Api137, drosocin and oncocin [74]. Oncocin became trapped within the endothelial cells of the brain capillaries, while the others made their way more efficiently into the brain parenchyma [74]. The subcellular location of IDR-1018 in the brain is currently not known and warrants further investigation. IDR-1018 has shown efficacy in murine models of cerebral hyoxia-ischemia [9] and cerebral malaria [10], which may be due to enhanced uptake of the peptide into the brain due to access across the BBB in those conditions; this has been observed with colistin and other HDPs previously [75–77].

Imaging of HDPs following IV administration to animals with soft tissue infections has shown that only a small fraction of the peptide distributes to the site of infection [49]. As a result, most HDPs in clinical

development [37–39,78], as well as pre-clinical studies with IDR-1018 [9–13,17–20], have focused on extravascular or local administration. We found that ^{67}Ga-NOTA-IDR-1018 was well-absorbed from a SQ injection site, with ~25% of the injected dose remaining at 4 h post-injection and ~5% between 21 and 48 h. The HDP A3-APO was not absorbed as quickly, with only ~20% ID within the blood pool 2 h after an intramuscular (IM) injection [79]. Fluorescent imaging of A3-APO following a SQ injection found that little peptide had distributed at 20 min post-injection [80]. Haney *et al.* [22] observed precipitation of IDR-1018 in the SQ tissue following a 8 mg/kg dose at 1 h post-injection. We did not observe any signs of precipitation in the SQ tissue at 3 mg/kg ^{67}Ga-NOTA-IDR-1018 when the injection site was visually examined after 48 h. Further study is necessary to see how absorption of IDR-1018 is impacted by precipitation and/or aggregation of the compound at high doses [17–19].

The mechanisms of action of IDR-1018 are to a degree concentration dependent, with anti-biofilm and immunomodulatory effects occurring at peptide concentrations lower than those required for direct antimicrobial effects. For example, only 5 μg/mL of IDR-1018 is required to influence macrophage polarization [7], and 20 μg/mL of the peptide can significantly alter the chemokine profile from PBMCs [5]. The minimal biofilm inhibitory concentration leading to 100% decrease in biofilm growth ranges from 2 to 10 μg/mL, depending on the pathogen [8]. MIC values against planktonic bacteria range from a low of 8 μg/mL against *Klebsiella pneumoniae* to >256 μg/mL against *Burkholderia cenocepacia*, with most other bacteria within the 32–64 μg/mL range [8]. At 2.5 mg/kg IV and 3 mg/kg SQ, only the SQ injection site had a high enough concentration of ^{67}Ga-NOTA-IDR-1018 to be above the MIC for most bacterial pathogens. This explains (in part) the effectiveness of local injections in treating SQ abscess models of infection [17–19]. IDR-1018 in other tissues likely exerts its therapeutic effects through modulation of the host immune system and a direct effect on the bacterial cells within the biofilm. Similar observations have been reported for other HDPs, such as Onc72, Onc112 and rhesus theta defensin 1. Following a 5 mg/kg IV bolus, the Onc HDPs were only above the MIC for *Escherichia coli* for 20–80 min post-injection, but still showed efficacy against the bacterium *in vivo* [55]. Maximum blood levels of rhesus theta defensin 1 following a 5 mg/kg IV bolus were nearly a tenth of the MIC for *Candida albicans* in a biological environment (100 μg/mL), but still showed efficacy in a candidiasis animal model [54].

HDPs, like IDR-1018, on their own have pharmacokinetic limitations that limit their efficacy and cause toxicity. New strategies need to be explored to overcome these issues. Simple changes, such as injecting HDPs as a gradual IV infusion instead of a bolus, may help to prevent lung toxicity and better sustain blood concentrations of IDR-1018. Steady blood concentrations can also be achieved with repeated extravascular dosing of HDPs; Basso *et al.* [54] found that daily intraperitoneal (IP) injections of rhesus theta defensin 1 effectively maintained blood concentrations of ~1 μg/mL for 7 days. SQ osmotic pumps can also be used to sustain high localized concentrations of HDPs and maintain steady blood concentrations [81,82]. Drug delivery systems could also help to prevent rapid clearance of HDPs directly injected into the blood. Example include PEGylation of SET-M33L [45], which increased the circulation half-life by 10-fold, and PEGylation of ubiquicidin 29–41 [67], which increased blood concentrations of the HDP by 20-fold at 2 h post-injection. Besides drug conjugates, nanoparticles have also shown some promise in modulating the pharmacokinetics of HDPs. For example, melittin incorporated into the outer lipid layer of a perfluorocarbon nanoparticle increased blood concentrations by 10-fold at 2 h post-injection [43,83]. A caveat is that although drug delivery systems might improve the circulation of HDPs in the blood, they have the potential to increase accumulation of the peptides in the reticuloendothelial system network, which may result in toxicity at these sites [43,67].

4. Conclusion

A radiotracer labeled form IDR-1018 was prepared in this study using the long-lived gamma-emitting radiometal gallium-67 to better define the pharmacokinetics of this synthetic peptide *in vivo*. In mice, ^{67}Ga-NOTA-IDR-1018 was rapidly cleared from the blood following a low dose IV bolus with a $t_{1/2\alpha}$ of a couple of minutes. Due to the high concentration of HDP in the blood upon first pass through the lung capillary network, and the ability of IDR-1018 to interact with cell membranes, a reservoir of peptide was formed in the lungs that helped sustain blood levels for several hours post-injection. As the IV dose increased, however, IDR-1018 perturbed the endothelial membranes of the lung capillaries to an extent where alveolar hemorrhaging occurred, causing mortality within a short period of time from respiratory failure. IV administered ^{67}Ga-NOTA-IDR-1018 was cleared predominantly through the organs of the reticuloendothelial system which may in part have reflected the peptide precipitating in the blood. Following a low dose SQ injection, ^{67}Ga-NOTA-IDR-1018 was rapidly absorbed and was almost completely excreted over a 48 h period. Renal clearance of the radiotracer was more predominant for the SQ route when compared to IV administration. Only the SQ injection site had a high enough concentration of ^{67}Ga-NOTA-IDR-1018 to exert a direct antimicrobial effect on many common bacterial pathogens. All other sites and tissues, in both the low dose SQ and IV groups, had peptide concentrations more in line with anti-biofilm and/or immunomodulatory effects. We conclude that for IDR-1018 to be applied as a therapeutic molecule, it is best suited for local delivery at the site of infection or inflammation. Further work in developing advanced peptide formulation strategies and improving on peptide design features, amongst other refinements, will be required to safely and effectively delivery IDR-1018 and other related synthetic IDR peptides systemically.

5. Experimental section

5.1. Materials and reagents

IDR-1018 (VRLIVAVRIWRR-NH_2) was obtained commercially from CPC Scientific (San Jose, CA, USA) at a purity ≥95%. S-(4-Isothiocyanatobenzyl)-1,4,7-triazacyclononane-1,4,7-triacetic acid (p-SCN-Bn-NOTA) was purchased from Macrocyclics (Plano, TX, USA) and ^{67}Ga-citrate was obtained from Isologic Innovative Radiopharmaceuticals (Dorval, QC, Canada). Tec-Control 150-771 ITLC strips were obtained from Biodex Medical Systems (Shirley, NY, USA). Sep-Pak vacuum cartridges pre-loaded with 100 mg of silica-gel sorbent were purchased from Waters Corporation (Milford, MA, USA). All supplies used to prepare and run the SDS-PAGE analysis were from Bio-Rad Laboratories (Hercules, CA, USA). Isoflurane USP was obtained from Fresenius Kabi Canada (Toronto, ON, Canada) and lactated Ringer's solution USP from Baxter Canada (Mississauga, ON, Canada). HUVEC cells were acquired from Lonza (Basal, Switzerland). Cell culture consumables were from USA Scientific (Ocala, FL, USA) or Corning (Corning, NY, USA), while all cell culture media and reagents were from Thermo Fisher Scientific (Waltham, MA, USA) or Lonza. All other reagents and solvents were purchased from MilliporeSigma (Burlington, MA, USA) and used as received without further purification. Type 1 ultrapure water from an in-house Milli-Q Integral 10 filtration system (MillporeSigma) was used in all experiments.

5.2. Preparation and characterization of ^{67}Ga-NOTA-IDR-1018

An aqueous solution of IDR-1018 (92 μL, 12 mg/mL, 0.72 μmol) was combined with $NaHCO_3$ (46 μL, 0.1 M); the pH of this solution was between 7 and 8 according to pH-indicator strips (MQuant, MilliporeSigma). p-SCN-Bn-NOTA in DMSO was then added (3.5 μL, 20 mg/mL, 0.13 μmol) and allowed to react overnight on an Eppendorf Thermomixer® set at 25 °C and 650 rpm.

The modified peptide was isolated using a 1 mL vacuum cartridge containing 100 mg of silica-gel sorbent (Waters Corporation; Milford, MA, USA). The cartridge was pre-conditioned using 0.5 mL methanol followed by 3 mL of water and was operated using positive pressure from an air-filled syringe and adapter seal. To load the cartridge, the crude reaction mixture was first diluted to a total volume of 1 mL with water and then slowly pushed through. The column was then washed thrice with 1 mL of water to remove unreacted chelator, solvents and salts. IDR-1018/NOTA-IDR-1018 was recovered from the cartridge using 0.25 mL fractions of 0.01 M HCl in water. The 2nd and 3rd acidic fractions were pooled and used for downstream radiolabeling reactions. Elution and peptide recovery were monitored by measuring the absorption of the fractions at 280 nm on the Nanodrop 2000 spectrophotometer (Thermo Fisher Scientific; Waltham, MA, USA).

^{67}Ga-citrate was concentrated and converted to $^{67}GaCl_3$ using a method adapted from Scasnar and van Lier [84]. Briefly, ^{67}Ga-citrate solution (192 MBq, 117 MBq/mL) was passed through a cartridge containing 100 mg of silica-gel sorbent pre-conditioned with methanol then water. The cartridge was washed with 3 mL of water to remove the citrate ions, and the radiometal was then eluted using 15% v/v 0.1 M HCl in acetone. After heating the eluent overnight at 40 °C in an open container, $^{67}GaCl_3$ in 0.1 M HCl remained. The activity concentration at the time of radiolabeling was 2.5 GBq/mL, an approximately 30-fold increase from the ^{67}Ga-citrate starting solution when corrected for decay.

NOTA-IDR-1018 in 0.01 M HCl (0.55 mL, 1.4 mg/mL) was combined with $^{67}GaCl_3$ in 0.1 M HCl (10 μL, 2.5 GBq/mL) and adjusted to pH 4–5 using a small amount of 1 M NaOH. The reaction was allowed to proceed on an Eppendorf Thermomixer® set at 20 °C and 750 rpm for 7 h.

Radiolabeling efficiency and purity was determined using an ITLC system consisting of a paper-based stationary phase and a 0.01 M EDTA in 0.9% w/v NaCl mobile phase. The location and amount of radioactivity on the strips was assessed using a Cyclone Phosphorimager and Optiquant software from Packard Instruments (Downers Grove, IL, USA).

The molecular weight of the radiotracer was assessed with SDS-PAGE using gels cast with a 20% w/v resolving phase and 4% stack [85]. Peptide samples (5 μL, 0.5 mg/mL) were mixed with an equal volume of twice-concentrated Laemmli buffer and heated at 95 °C for 5 min. The samples, namely unmodified and radiolabeled IDR-1018, were then loaded onto the gel along with a pre-stained ladder (Precision Plus Protein Kaleidoscope, Bio-Rad Laboratories) as a molecular weight reference. The gel was run in Tris/glycine/SDS buffer using a Mini-PROTEAN Tetra Cell and PowerPac HV power supply from Bio-Rad Laboratories. Bands were visualized using Brilliant-Blue R-250 (Coomassie) stain. The gels were documented on an Odyssey CLx Imager (LiCor, USA) set at 700 nm excitation and analyzed using Image Studio software that accompanied the instrument.

5.3. Animals and ethics statement

All animal experiments were performed in accordance with the Canadian Council on Animal Care (CCAC) under an approved protocol (A16-0150) by the Animal Care Committee (ACC) of the University of British Columbia.

Healthy female C57Bl/6 mice (Strain code 027) with a weight between 22 and 25 g were obtained from Charles Rivers Laboratories (Wilmington, MA, USA) and housed in a controlled environment (22 °C, 12 h day/night cycle). The animals had unlimited access to enrichment, food and water. They were acclimatized to the facility for a minimum of 1 week before use.

5.4. SPECT/CT and biodistribution studies

In preparation for administration, the ^{67}Ga-NOTA-IDR-1018 solution was adjusted to ~pH 5–6 with a small amount of 1 M NaOH and to isotonicity using an appropriate amount of 9% w/v NaCl. To achieve the desired peptide dose in a volume of 100 μL, ^{67}Ga-NOTA-IDR-1018 was either i) diluted with 0.9% w/v NaCl (normal saline) or ii) spiked with unmodified IDR-1018 in normal saline. Each dose contained roughly 1.5 MBq of activity and were loaded into 29 G insulin syringes (Becton Dickinson; Franklin Lakes, NJ, USA) for administration.

Mice were randomly allocated into IV and SQ groups. Each mouse was anesthetized with isoflurane in oxygen (5% induction, 1.5–2% maintenance) using a RC^2 rodent precision vaporizer (VetEquip; Pleasanton, CA, USA) and provided with 0.5 mL of SQ Ringer's lactated solution for hydration prior to radiotracer administration (and each subsequent scan). IV doses were injected as a bolus via the tail vein and SQ injections were administered on the flank. A dose calibrator (CRC-55tR, Capintec; Florham Park, FL, USA) was used to measure the syringes before and after injection to determine the final administered dose.

After injection of the radiotracer, the mice were immediately scanned in list-mode under isoflurane anesthesia (1.5–2% in oxygen) on a VECTor/CT multimodal pre-clinical scanner outfitted with an extra-ultra-high sensitivity (XUHS) mouse pinhole collimator (MILabs; Houten, The Netherlands) [86,87]. A CT scan was acquired following the SPECT acquisition (1 frame, 180 projections over 360°) using tube settings of 55 kV and 615 μA. Animals were recovered with heat and hydration support before being returned to their cage. Each animal was scanned up to 5 times over a 48 h period, as summarized in **Table S2**.

The CT projection data was reconstructed using SkyScan NRecon software (Microphotonics Inc.; Allentown, PA, USA) to generate a 3D image with a 0.169 mm^3 voxel size. SPECT data was reconstructed using a pixel-ordered subset expectation maximization (POSEM) algorithm using 16 subsets, 6 iterations and an isotropic 0.4 mm voxel grid with U-SPECT Rec2.5li software (MILabs). The 79 keV photopeak of ^{67}Ga with a 20% energy window width was used for the reconstruction. The SPECT files were decay corrected to the start of each scan and after CT registration, attenuation correction was applied using U-SPECT Rec2.5li software.

The SPECT dataset was quantified using AMIDE software (UCLA; Los Angeles, CA, USA) [88]. Spherical volumes of interest (VOIs) with a diameter of 1.5 mm were drawn in the left ventricle of the heart (blood pool), liver, kidney, spleen, lung and 4 different locations of the skeleton: femur, vertebrae and the knee and shoulder regions. VOIs were also placed over the urinary bladder, injection site and whole animal. A calibration factor, obtained by scanning a point source phantom containing a known concentration of ^{67}Ga, was used to convert the VOI data from scanner units (counts/voxel) to units of radioactivity concentration (MBq/mL). VOI data were decay corrected to the time of injection of the radiotracer. VOI data are presented as SUV_{mean}, which was calculated using Equation 1.

$$SUV_{mean}\,(g/mL) = \frac{mean\ radioactivity\ concentration\ in\ VOI\ (MBq/mL)\ x\ weight\ of\ animal\ (g)}{injected\ radioactive\ dose\ (MBq)}$$

Equation 1: SUV formula for SPECT analysis.

Tissue concentration activities were at times also reported in units of % ID/g and μg/g. The former was calculated according to Equation 2 using standardized densities for mouse tissues [89,90] and body fluids [91,92]. The latter was obtained using Equation 3. For body fluids, namely the urine and blood, μg/g was multiplied by the density of the fluid to report μg/mL.

$$\%\,ID/g = \frac{mean\ radioactivity\ concentration\ in\ VOI\ (MBq/mL)}{injected\ radioactive\ dose\ (MBq)\ x\ organ\ density\ (g/mL)}\ x\,100$$

Equation 2: % ID/g formula for SPECT analysis.

$$\mu g/g = \frac{\%\,ID/g\ x\ peptide\ dose\ (\mu g)}{100}$$

Equation 3: μg/g formula for SPECT analysis.

% ID/ organ was calculated by multiplying % ID/g by the weight of the organ. For organs that could not be fully removed and weighed, such as the blood, standardized organ weights were used [93,94]. The proportion of the injected dose remaining within a particular volume, such as the injection site or urinary bladder, was determined according to Equation 4.

$$\%\,ID = \frac{mean\ radioactivity\ concentration\ in\ VOI\ (MBq/mL)\ x\ VOI\ volume\ (mL)}{injected\ radioactive\ dose\ (MBq)}\ x\,100$$

Equation 4: % ID formula for SPECT analysis.

5.5. Pharmacokinetic modeling

Microsoft Excel 2016 (Redmond, WA, USA) with the add-in PKSolver [95] was used to perform IV bolus and extravascular non-compartmental modeling from the blood concentration. T_{max}, C_{max}, $AUC_{0\text{-}\infty}$, and $MRT_{0\text{-}\infty}$ are reported.

5.6. Biodistribution

Following the final SPECT/CT scan, the animals were kept under isoflurane anesthesia and promptly sacrificed using a 2-step process: (i) cardiac puncture to obtain a blood sample followed by (ii) CO_2 asphyxiation. The activity in the carcass was recorded using a CRC-55tR dose calibrator and organs/tissue samples were harvested via dissection. The samples were then weighed and the amount of radioactivity within them measured using a Cobra II 5010 gamma counter (Packard Instruments) recording counts per minute (cpm) of photons between 15 and 2000 keV. A calibration factor was applied to convert cpm values into units of radioactivity (MBq). Data is reported as percentage of the % ID/g and % ID/organ. For organs that could not be completely removed via dissection for analysis, such as the skeleton and blood, % ID/organ values were obtained by multiplying the obtained % ID/g value by standardized organ weights or volumes for age- and sex-matched mice [93,94].

5.7. Histological assessments

Mice were administered unmodified IDR-1018 at 8 mg/kg (n = 2) and 15 mg/kg (n = 2) in 100 μL of normal saline as an IV bolus via the tail vein. A control animal (n = 1) received a 100 μL IV bolus of normal saline. The injections were performed under isoflurane anesthesia (5% in oxygen for induction, 2% in oxygen for maintenance).

The time to respiratory arrest was recorded and the mice were then cervically dislocated. The heart and lungs were removed as a plug (i.e., connected to each other) and fixed over a 3 day period in 10% neutral buffered formalin (NBF) at room temperature. The samples were embedded in paraffin, sectioned (4 μm thickness), mounted on glass slides and stained with hematoxylin and eosin (H&E) using well-established protocols at the histology core at the UBC Centre for Comparative Medicine.

The slides were provided to a veterinary pathologist for examination (Animal Pathology Services Ltd; Edmonton, AB, Canada). The pathologist was not affiliated with the project and blinded as to the experimental group of the mice, so as to obtain an unbiased opinion. Representative light micrographs at 100× and 400× were provided of the lungs and heart of IDR-1018 treated and control animals.

5.8. Cell morphology

HUVEC cells were cultured in endothelial growth medium (EGM), which was prepared using an EGM-2 Bullet Kit and maintained at 37 °C in a humidified 5% CO_2 incubator. Cells were grown to approximately 70–80% confluence and detached with trypsin-EDTA in order to be passaged or seeded for an experiment. The cells were passaged at least twice after being thawed for used in experiments.

HUVEC cells were seeded into 96-well plates at a density of 5000 cells per well in 100 μL of complete media and allowed to adhere overnight. IDR-1018 was then added in triplicate in 100 μL of media to a final concentration between 0 and 300 μg/mL in the well. Phase contrast images at 10X magnification were immediately taken using an Incucyte ZOOM live cell imager (Essen Bioscience; Ann Arbor, Michigan, USA). Data is reported as representative micrographs, which were prepared using Incucyte ZOOM 2016A software (Essen Bioscience).

5.9. Graphing and image rendering

OriginPro 2020 software (OriginLab Corporation; Northampton, MA, USA) was used to digitize ITLC traces. Prism 8 software (GraphPad Software; San Diego, CA, USA) was used for all graphing and curve fitting. AMIDE software was used to overlay the SPECT and CT files and generate fused 2D images and 3D maximum intensity projection (MIP) renderings; SPECT data was Gaussian filtered using a kernel size of 19 and Full Width at Half Maximum (FWHM) of 1 mm. Chemical structures were drawn using ChemBioDraw Ultra 13 software (PerkinElmer; Waltham, MA, USA) and the graphical abstract was created partly using BioRender.com (Toronto, ON, Canada). Multi-panel figures were prepared using Illustrator CC 2015 software (Adobe; San Jose, CA, USA).

CRediT authorship contribution statement

Tullio V.F. Esposito: Conceptualization, Methodology, Validation, Formal analysis, Investigation, Writing – original draft, Visualization, Project administration. **Cristina Rodríguez-Rodríguez:** Investigation. **Colin Blackadar:** Investigation. **Evan F. Haney:** Writing – review & editing. **Daniel Pletzer:** Conceptualization, Writing – original draft, Writing – review & editing, Visualization, Supervision, Project administration. **Robert E.W. Hancock:** Resources, Writing – review & editing, Supervision, Funding acquisition. **Katayoun Saatchi:** Methodology, Validation, Investigation, Writing – review & editing, Supervision. **Urs**

O. Häfeli: Resources, Writing – review & editing, Supervision.

Declaration of Competing Interest

The authors declare the following financial interests/personal relationships which may be considered as potential competing interests: EFH and REWH have invented and filed for patent protection on IDR-1018 and related peptide sequences. This patent has been assigned to their employer, the University of British Columbia, and has been licensed to ABT Innovations Inc., in which both have an ownership position. ABT Innovations Inc. is a subsidiary of ASEP Medical Holdings Inc. EFH is employed by ASEP and receives salary while REWH holds an executive position and is on the Board of ASEP.

TVFE, CB, DP, CRR, KS and UOH report no conflicts of interest.

Acknowledgments

This research was made possible by grants from the Lundbeck Foundation of Denmark (Lundbeck Foundation Professorship to UOH, No. 2014-4176), the Natural Sciences and Engineering Research Council of Canada (NSERC, Discovery Grant to UOH, No. 2018-04958) and the Canadian Institutes of Health Research (CIHR, Foundation Grant to REWH, No. FDN-154287). Funding for the VECTor preclinical imaging platform at the UBC *in vivo* Imaging Centre was provided through a grant, in part to UOH, from the Canada Foundation for Innovation (CFI, No. 25413). KS acknowledges the support of Isologic Radiopharmaceutiques Novatuers for the supply of the radioisotope.

REWH held a Canada Research Chair in Health and Genomics and a UBC Killam Professorship. TVFE received support from a Killam Doctoral Fellowship and a 4YF Fellowship from the University of British Columbia (UBC). CB received support from NSERC via an Undergraduate Student Research Award (USRA). DP received a Cystic Fibrosis Canada Postdoctoral Fellowship and a Michael Smith Foundation for Health Research - Research Trainee Award.

We would like to thank Maryam Osooly for helping to administer the radiotracers intravenously. We are grateful to the veterinary staff, particularly Dr. Laura Mowbray, at the UBC Center for Comparative Medicine (CCM) for all their support during animal studies. And finally, we would like to thank Jana Hodasova from UBC CCM for all the help and expertise she provided with the histology studies.

Appendix A. Supplementary material

Supplementary data to this article can be found online at https://doi.org/10.1016/j.ejpb.2022.08.004.

References

[1] M. Zasloff, Antimicrobial peptides of multicellular organisms, Nature 415 (2002) 389–395.
[2] E.F. Haney, S.C. Mansour, R.E.W. Hancock, Antimicrobial Peptides: An Introduction, in: P.R. Hansen (Ed.) Antimicrobial Peptides: Methods and Protocols, Springer New York, New York, NY, 2017, pp. 3–22.
[3] E.F. Haney, S.K. Straus, R.E.W. Hancock, Reassessing the host defense peptide landscape, Front. Chem. 7 (2019).
[4] S.C. Mansour, C. de la Fuente-Núñez, R.E.W. Hancock, Peptide IDR-1018: modulating the immune system and targeting bacterial biofilms to treat antibiotic-resistant bacterial infections, J. Pept. Sci. 21 (2015) 323–329.
[5] M. Wieczorek, H. Jenssen, J. Kindrachuk, W.R. Scott, M. Elliott, K. Hilpert, J.T. Cheng, R.E. Hancock, S.K. Straus, Structural studies of a peptide with immune modulating and direct antimicrobial activity, Chem. Biol. (Oxford, U. K.), 17 (2010) 970–980.
[6] F. Niyonsaba, L. Madera, N. Afacan, K. Okumura, H. Ogawa, R.E. Hancock, The innate defense regulator peptides IDR-HH2, IDR-1002, and IDR-1018 modulate human neutrophil functions, J. Leukocyte Biol. 94 (2013) 159–170.
[7] O.M. Pena, N. Afacan, J. Pistolic, C. Chen, L. Madera, R. Falsafi, C.D. Fjell, R.E. W. Hancock, Synthetic cationic peptide IDR-1018 modulates human macrophage differentiation, PLoS ONE 8 (2013) e52449.
[8] C. de la Fuente-Núñez, F. Reffuveille, E.F. Haney, S.K. Straus, R.E. Hancock, Broad-spectrum anti-biofilm peptide that targets a cellular stress response, PLoS Pathog. 10 (2014) e1004152.
[9] H. Bolouri, K. Savman, W. Wang, A. Thomas, N. Maurer, E. Dullaghan, C.D. Fjell, C. J. Ek, H. Hagberg, R.E. Hancock, K.L. Brown, C. Mallard, Innate defense regulator peptide 1018 protects against perinatal brain injury, Ann. Neurol. 75 (2014) 395–410.
[10] A.H. Achtman, S. Pilat, C.W. Law, D.J. Lynn, L. Janot, M.L. Mayer, S. Ma, J. Kindrachuk, B.B. Finlay, F.S. Brinkman, G.K. Smyth, R.E. Hancock, L. Schofield, Effective adjunctive therapy by an innate defense regulatory peptide in a preclinical model of severe malaria, Sci. Transl. Med. 4 (2012) 135ra164.
[11] B. Rivas-Santiago, J.E. Castañeda-Delgado, C.E. Rivas Santiago, M. Waldbrook, I. González-Curiel, J.C. León-Contreras, J.A. Enciso-Moreno, V.d. Villar, J. Mendez-Ramos, R.E.W. Hancock, R. Hernandez-Pando, Ability of innate defence regulator peptides IDR-1002, IDR-HH2 and IDR-1018 to protect against mycobacterium tuberculosis infections in animal models, PLOS ONE 8 (2013) e59119.
[12] H. Choe, A.S. Narayanan, D.A. Gandhi, A. Weinberg, R.E. Marcus, Z. Lee, R. A. Bonomo, E.M. Greenfield, Immunomodulatory peptide IDR-1018 decreases implant infection and preserves osseointegration, Clin. Orthop. Relat. Res. 473 (2015) 2898–2907.
[13] L. Steinstraesser, T. Hirsch, M. Schulte, M. Kueckelhaus, F. Jacobsen, E.A. Mersch, I. Stricker, N. Afacan, H. Jenssen, R.E.W. Hancock, J. Kindrachuk, Innate defense regulator peptide 1018 in wound healing and wound infection, PLoS ONE 7 (2012) e39373.
[14] P. Marin-Luevano, V. Trujillo, A. Rodriguez-Carlos, I. Gonzalez-Curiel, J.A. Enciso-Moreno, R.E.W. Hancock, B. Rivas-Santiago, Induction by innate defence regulator peptide 1018 of pro-angiogenic molecules and endothelial cell migration in a high glucose environment, Peptides 101 (2018) 135–144.
[15] T. Alencar-Silva, A. Zonari, D. Foyt, M. Gang, R. Pogue, F. Saldanha-Araujo, S. C. Dias, O.L. Franco, J.L. Carvalho, IDR-1018 induces cell proliferation, migration, and reparative gene expression in 2D culture and 3D human skin equivalents, J. Tissue Eng. Regener. Med. 13 (2019) 2018–2030.
[16] K. Yanashima, P. Chieosilapatham, E. Yoshimoto, K. Okumura, H. Ogawa, F. Niyonsaba, Innate defense regulator IDR-1018 activates human mast cells through g protein-, phospholipase C-, MAPK- and NF-κB-sensitive pathways, Immunol. Res. 65 (2017) 920–931.
[17] D. Pletzer, H. Wolfmeier, M. Bains, R.E.W. Hancock, Synthetic peptides to target stringent response-controlled virulence in a pseudomonas aeruginosa murine cutaneous infection model, Front. Microbiol. 8 (2017) 1867.
[18] D. Pletzer, S.C. Mansour, R.E.W. Hancock, Synergy between conventional antibiotics and anti-biofilm peptides in a murine, sub-cutaneous abscess model caused by recalcitrant ESKAPE pathogens, PLoS Pathog. 14 (2018) e1007084.
[19] Y. Cao, H. Yin, W. Wang, P. Pei, Y. Wang, X. Wang, J. Jiang, S.-Z. Luo, L. Chen, Killing streptococcus mutans in mature biofilm with a combination of antimicrobial and antibiofilm peptides, Amino Acids 52 (2020) 1–14.
[20] S.R. Coleman, D. Pletzer, R.E.W. Hancock, Contribution of swarming motility to dissemination in a pseudomonas aeruginosa murine skin abscess infection model, J. Infect. Dis. 224 (2020) 726–733.
[21] L.V. Wilkinson, M.A. Alford, S.R. Coleman, B.C. Wu, A.H.Y. Lee, T.M. Blimkie, M. Bains, R. Falsafi, D. Pletzer, R.E.W. Hancock, Peptide 1018 inhibits swarming and influences Anr-regulated gene expression downstream of the stringent stress response in Pseudomonas aeruginosa, PLoS ONE 16 (2021) e0250977.
[22] E.F. Haney, K.C. Wuerth, N. Rahanjam, N. Safaei Nikouei, A. Ghassemi, M. Alizadeh Noghani, A. Boey, R.E.W. Hancock, Identification of an IDR peptide formulation candidate that prevents peptide aggregation and retains immunomodulatory activity, Pept. Sci. 111 (2019) e24077.
[23] E.F. Haney, B. Wu, K. Lee, A.L. Hilchie, R.E.W. Hancock, Aggregation and its influence on the immunomodulatory activity of synthetic innate defense regulator peptides, Cell Chem. Biol. 24 (2017) 969–980.e964.
[24] R.E. Hancock, H.G. Sahl, Antimicrobial and host-defense peptides as new anti-infective therapeutic strategies, Nat. Biotechnol. 24 (2006) 1551–1557.
[25] E. Boros, C.L. Ferreira, J.F. Cawthray, E.W. Price, B.O. Patrick, D.W. Wester, M. J. Adam, C. Orvig, Acyclic chelate with ideal properties for (68)Ga PET imaging agent elaboration, J Am Chem Soc 132 (2010) 15726–15733.
[26] D. Blok, R.I. Feitsma, P. Vermeij, E.J. Pauwels, Peptide radiopharmaceuticals in nuclear medicine, Eur. J. Nucl. Med. 26 (1999) 1511–1519.
[27] M.S. Cooper, M.T. Ma, K. Sunassee, K.P. Shaw, J.D. Williams, R.L. Paul, P. S. Donnelly, P.J. Blower, Comparison of (64)Cu-complexing bifunctional chelators for radioimmunoconjugation: labeling efficiency, specific activity, and in vitro/in vivo stability, Bioconjugate Chem. 23 (2012) 1029–1039.
[28] J.M. Esteban, J. Schlom, O.A. Gansow, R.W. Atcher, M.W. Brechbiel, D.E. Simpson, D. Colcher, New method for the chelation of indium-111 to monoclonal antibodies: biodistribution and imaging of athymic mice bearing human colon carcinoma xenografts, J. Nucl. Med. 28 (1987) 861–870.
[29] L. Lang, W. Li, N. Guo, Y. Ma, L. Zhu, D.O. Kiesewetter, B. Shen, G. Niu, X. Chen, Comparison study of [18F]FAl-NOTA-PRGD2, [18F]FPPRGD2, and [68Ga]Ga-NOTA-PRGD2 for PET imaging of U87MG tumors in mice, Bioconjugate Chem. 22 (2011) 2415–2422.
[30] M.M. Herth, S. Ametamey, D. Antuganov, A. Bauman, M. Berndt, A.F. Brooks, G. Bormans, Y.S. Choe, N. Gillings, U.O. Häfeli, M.L. James, K. Kopka, V. Kramer, R. Krasikova, J. Madsen, L. Mu, B. Neumaier, M. Piel, F. Rösch, T. Ross, R. Schibli, P.J.H. Scott, V. Shalgunov, N. Vasdev, W. Wadsak, B.M. Zeglis, On the consensus nomenclature rules for radiopharmaceutical chemistry – Reconsideration of radiochemical conversion, Nucl. Med. Biol. 93 (2021) 19–21.
[31] J.A. Thie, Understanding the standardized uptake value its methods, and implications for usage, J. Nucl. Med. 45 (2004) 1431.
[32] U. Ziegler, P. Groscurth, Morphological features of cell death, Physiology 19 (2004) 124–128.

[33] M.-H. Sohn, B.J. Jones, J.H. Whiting, F.L. Datz, R.E. Lynch, K.A. Morton, Distribution of gallium-67 in normal and hypotransferrinemic tumor-bearing mice, J. Nucl. Med. 34 (1993) 2135–2143.

[34] L.R. Bernstein, Mechanisms of therapeutic activity for gallium, Pharmacol. Rev. 50 (1998) 665–682.

[35] T.V.F. Esposito, Rodriguez-Rodriguez, C., Blackadar, C., Saatchi, K., Hafeli, U. O., Pharmacokinetics of the Host Defense Peptide LL-37 using SPECT/CT, [In Preparation].

[36] C.L. Ferreira, E. Lamsa, M. Woods, Y. Duan, P. Fernando, C. Bensimon, M. Kordos, K. Guenther, P. Jurek, G.E. Kiefer, Evaluation of bifunctional chelates for the development of gallium-based radiopharmaceuticals, Bioconjug. Chem. 21 (2010) 531–536.

[37] N. Mookherjee, M.A. Anderson, H.P. Haagsman, D.J. Davidson, Antimicrobial host defence peptides: functions and clinical potential, Nat. Rev. Drug Discovery 19 (2020) 311–332.

[38] A.K. Marr, W.J. Gooderham, R.E.W. Hancock, Antibacterial peptides for therapeutic use: obstacles and realistic outlook, Curr. Opin. Pharmacol. 6 (2006) 468–472.

[39] K. Bush, M. Macielag, M. Weidner-Wells, Taking inventory: antibacterial agents currently at or beyond phase 1, Curr. Opin. Microbiol. 7 (2004) 466–476.

[40] C. Domhan, P. Uhl, C. Kleist, S. Zimmermann, F. Umstätter, K. Leotta, W. Mier, M. Wink, Replacement of l-amino acids by d-amino acids in the antimicrobial peptide ranalexin and its consequences for antimicrobial activity and biodistribution, Molecules (Basel Switzerland) 24 (2019).

[41] T.A. Aweda, Z.F.B. Muftuler, A.V.F. Massicano, D. Gadhia, K.A. McCarthy, S. Queern, A. Bandyopadhyay, J. Gao, S.E. Lapi, Radiolabeled Cationic Peptides for Targeted Imaging of Infection, Contrast Media Mol. Imaging 2019 (2019) 3149249.

[42] J. Yuan, X. You, G. Ni, T. Wang, S. Cavezza, X. Pan, X. Liu, Iodine-125 labeled Australian frog tree host-defense peptides caerin 1.1 and 1.9 better inhibit human breast cancer cells growth than the unlabeled peptides. (125)I-caerin 1.9 may better be used for the treatment of breast cancer, Hellenic J. Nucl. Med. 21 (2018) 115-120.

[43] N.R. Soman, S.L. Baldwin, G. Hu, J.N. Marsh, G.M. Lanza, J.E. Heuser, J.M. Arbeit, S.A. Wickline, P.H. Schlesinger, Molecularly targeted nanocarriers deliver the cytolytic peptide melittin specifically to tumor cells in mice, reducing tumor growth, J. Clin. Invest. 119 (2009) 2830–2842.

[44] J.S.M. Svendsen, T.M. Grant, D. Rennison, M.A. Brimble, J. Svenson, Very short and stable lactoferricin-derived antimicrobial peptides: design principles and potential uses, Acc. Chem. Res. 52 (2019) 749–759.

[45] J. Brunetti, C. Falciani, G. Roscia, S. Pollini, S. Bindi, S. Scali, U.C. Arrieta, V. Gómez-Vallejo, L. Quercini, E. Ibba, M. Prato, G.M. Rossolini, J. Llop, L. Bracci, A. Pini, In vitro and in vivo efficacy, toxicity, bio-distribution and resistance selection of a novel antibacterial drug candidate, Sci. Rep. 6 (2016) 26077.

[46] S.K. Puttrevu, T.S. Laxman, A.K. Tripathi, A.K. Yadav, S.K. Verma, A. Mishra, R. Pradhan, N.K. Verma, J.K. Ghosh, R.S. Bhatta, Liquid chromatography–tandem mass spectrometry based method development and validation of S016–1271 (LR8P), a novel cationic antimicrobial peptide for its application to pharmacokinetic studies, J. Pharm. Biomed. Anal. 169 (2019) 116–126.

[47] F.E. Ali, G. Cao, A. Poudyal, T. Vaara, R.L. Nation, M. Vaara, J. Li, Pharmacokinetics of novel antimicrobial cationic peptides NAB 7061 and NAB 739 in rats following intravenous administration, J. Antimicrob. Chemother. 64 (2009) 1067–1070.

[48] W.J.F.M. van der Velden, T.M.P. van Iersel, N.M.A. Blijlevens, J.P. Donnelly, Safety and tolerability of the antimicrobial peptide human lactoferrin 1–11 (hLF1-11), BMC Med. 7 (2009) 44.

[49] M.M. Welling, P.H. Nibbering, A. Paulusma-Annema, P.S. Hiemstra, E.K. Pauwels, W. Calame, Imaging of bacterial infections with 99mTc-labeled human neutrophil peptide-1, Journal of nuclear medicine : official publication, Soc. Nucl. Med. 40 (1999) 2073–2080.

[50] C.P.J.M. Brouwer, S.J.P. Bogaards, M. Wulferink, M.P. Velders, M.M. Welling, Synthetic peptides derived from human antimicrobial peptide ubiquicidin accumulate at sites of infections and eradicate (multi-drug resistant) Staphylococcus aureus in mice, Peptides 27 (2006) 2585–2591.

[51] M.S. Akhtar, A. Qaisar, J. Irfanullah, J. Iqbal, B. Khan, M. Jehangir, M.A. Nadeem, M.A. Khan, M.S. Afzal, I. Ul-Haq, M.B. Imran, Antimicrobial peptide 99mTc-ubiquicidin 29–41 as human infection-imaging agent: clinical trial, J. Nucl. Med.: Official Publ. Soc. Nucl. Med. 46 (2005) 567–573.

[52] E. Teyssières, J.P. Corre, S. Antunes, C. Rougeot, C. Dugave, G. Jouvion, P. Claudon, G. Mikaty, C. Douat, P.L. Goossens, G. Guichard, Proteolytically Stable foldamer mimics of host-defense peptides with protective activities in a murine model of bacterial infection, J. Med. Chem. 59 (2016) 8221–8232.

[53] G. Wu, S. Wang, X. Wang, X. Li, X. Deng, Z. Shen, T. Xi, Determination of a new antibacterial peptide S-thanatin in rat plasma by an indirected-ELISA, Peptides 32 (2011) 1484–1487.

[54] V. Basso, D.Q. Tran, J.B. Schaal, P. Tran, Y. Eriguchi, D. Ngole, A.E. Cabebe, A.Y. Park, P.M. Beringer, A.J. Ouellette, M.E. Selsted, Rhesus theta defensin 1 promotes long term survival in systemic candidiasis by host directed mechanisms, Sci. Rep. 9 (2019) 16905–16905.

[55] R. Schmidt, E. Ostorházi, E. Wende, D. Knappe, R. Hoffmann, Pharmacokinetics and in vivo efficacy of optimized oncocin derivatives, J. Antimicrob. Chemother. 71 (2016) 1003–1011.

[56] J. Knust, M. Ochs, H.J. Gundersen, J.R. Nyengaard, Stereological estimates of alveolar number and size and capillary length and surface area in mice lungs, Anatomical. Rec. (Hoboken N.J.) 292 (2009) (2007) 113–122.

[57] R. Bucki, K. Niemirowicz, U. Wnorowska, F.J. Byfield, E. Piktel, M. Wątek, P. A. Janmey, P.B. Savage, Bactericidal activity of ceragenin CSA-13 in Cell culture and in an animal model of peritoneal infection, Antimicrob. Agents Chemother. 59 (2015) 6274–6282.

[58] J. Svenson, B.O. Brandsdal, W. Stensen, J.S. Svendsen, Albumin binding of short cationic antimicrobial micropeptides and its influence on the in vitro bactericidal effect, J. Med. Chem. 50 (2007) 3334–3339.

[59] Y. Wang, J. Johansson, B. Agerberth, H. Jörnvall, W.J. Griffiths, The antimicrobial peptide LL-37 binds to the human plasma protein apolipoprotein A-I, Rapid Commun. Mass Spectrom.: RCM 18 (2004) 588–589.

[60] Y.E. Lau, A. Rozek, M.G. Scott, D.L. Goosney, D.J. Davidson, R.E. Hancock, Interaction and cellular localization of the human host defense peptide LL-37 with lung epithelial cells, Infect. Immun. 73 (2005) 583–591.

[61] H.B. Yu, A. Kielczewska, A. Rozek, S. Takenaka, Y. Li, L. Thorson, R.E.W. Hancock, M.M. Guarna, J.R. North, L.J. Foster, O. Donini, B.B. Finlay, Sequestosome-1/p62 is the key intracellular target of innate defense regulator peptide, J. Biol. Chem. 284 (2009) 36007–36011.

[62] A. Nijnik, L. Madera, S. Ma, M. Waldbrook, M.R. Elliott, D.M. Easton, M.L. Mayer, S.C. Mullaly, J. Kindrachuk, H. Jenssen, R.E. Hancock, Synthetic cationic peptide IDR-1002 provides protection against bacterial infections through chemokine induction and enhanced leukocyte recruitment, J. Immunol. (Baltimore Md.) 184 (2010) (1950) 2539–2550.

[63] L. Steinstraesser, T. Hirsch, M. Schulte, M. Kueckelhaus, F. Jacobsen, E.A. Mersch, I. Stricker, N. Afacan, H. Jenssen, R.E.W. Hancock, J. Kindrachuk, Innate defense regulator peptide 1018 in wound healing and wound infection, PLoS One 7 (2012) e39373–e39373.

[64] M. Wieczorek, H. Jenssen, J. Kindrachuk, W.R. Scott, M. Elliott, K. Hilpert, J. T. Cheng, R.E. Hancock, S.K. Straus, Structural studies of a peptide with immune modulating and direct antimicrobial activity, Chem. Biol. 17 (2010) 970–980.

[65] P.G. Barlow, Y. Li, T.S. Wilkinson, D.M.E. Bowdish, Y.E. Lau, C. Cosseau, C. Haslett, A.J. Simpson, R.E.W. Hancock, D.J. Davidson, The human cationic host defense peptide LL-37 mediates contrasting effects on apoptotic pathways in different primary cells of the innate immune system, J Leukoc. Biol. 80 (2006) 509–520.

[66] A. Lupetti, M.M. Welling, U. Mazzi, P.H. Nibbering, E.K. Pauwels, Technetium-99m labelled fluconazole and antimicrobial peptides for imaging of Candida albicans and Aspergillus fumigatus infections, Eur. J. Nucl. Med. Mol. Imaging 29 (2002) 674–679.

[67] L. Meléndez-Alafort, A. Nadali, G. Pasut, E. Zangoni, R. De Caro, L. Cariolato, M. C. Giron, I. Castagliuolo, F.M. Veronese, U. Mazzi, Detection of sites of infection in mice using 99mTc-labeled PN(2)S-PEG conjugated to UBI and 99mTc-UBI: a comparative biodistribution study, Nucl. Med. Biol. 36 (2009) 57–64.

[68] H.H. Gustafson, D. Holt-Casper, D.W. Grainger, H. Ghandehari, Nanoparticle uptake: the phagocyte problem, Nano Today 10 (2015) 487–510.

[69] S. Nie, Understanding and overcoming major barriers in cancer nanomedicine, Nanomedicine (London U.K.) 5 (2010) 523–528.

[70] D.S. Kohane, Microparticles and nanoparticles for drug delivery, Biotechnol. Bioeng. 96 (2007) 203–209.

[71] A. Ruggiero, C.H. Villa, E. Bander, D.A. Rey, M. Bergkvist, C.A. Batt, K. Manova-Todorova, W.M. Deen, D.A. Scheinberg, M.R. McDevitt, Paradoxical glomerular filtration of carbon nanotubes, Proc. Natl. Acad. Sci. U.S.A. 107 (2010) 12369–12374.

[72] B. Du, X. Jiang, A. Das, Q. Zhou, M. Yu, R. Jin, J. Zheng, Glomerular barrier behaves as an atomically precise bandpass filter in a sub-nanometre regime, Nat. Nanotechnol. 12 (2017) 1096–1102.

[73] S.A. Hitchcock, Blood–brain barrier permeability considerations for CNS-targeted compound library design, Curr. Opin. Chem. Biol. 12 (2008) 318–323.

[74] S. Stalmans, E. Wynendaele, N. Bracke, D. Knappe, R. Hoffmann, K. Peremans, I. Polis, C. Burvenich, B. De Spiegeleer, Blood-brain barrier transport of short proline-rich antimicrobial peptides, Protein Pept. Lett. 21 (2014) 399–406.

[75] M.E. Jiménez-Mejías, C. Pichardo-Guerrero, F.J. Márquez-Rivas, D. Martín-Lozano, T. Prados, J. Pachón, Cerebrospinal fluid penetration and pharmacokinetic/pharmacodynamic parameters of intravenously administered colistin in a case of multidrug-resistant Acinetobacter baumannii meningitis, Euro. J. Clin. Microbiol. Infect. Diseases: Off. Publ. Euro. Soc. Clin. Microbiol. 21 (2002) 212–214.

[76] V.J. Quagliarello, W.M. Scheld, New perspectives on bacterial meningitis, Clin. Infect. Diseases: Off. Publ. Infect. Diseases Soc. Am. 17 (1993) 603–608; quiz 609-610.

[77] L. Liu, K. Xu, H. Wang, P.K. Tan, W. Fan, S.S. Venkatraman, L. Li, Y.Y. Yang, Self-assembled cationic peptide nanoparticles as an efficient antimicrobial agent, Nat. Nanotechnol. 4 (2009) 457–463.

[78] G.S. Dijksteel, M.M.W. Ulrich, E. Middelkoop, B.K.H.L. Boekema, Review: lessons learned from clinical trials using Antimicrobial Peptides (AMPs), Front. Microbiol. 12 (2021).

[79] E. Ostorhazi, F. Rozgonyi, A. Sztodola, F. Harmos, I. Kovalszky, D. Szabo, D. Knappe, R. Hoffmann, M. Cassone, J.D. Wade, R.A. Bonomo, L. Otvos Jr., Preclinical advantages of intramuscularly administered peptide A3-APO over existing therapies in Acinetobacter baumannii wound infections, J. Antimicrob. Chemother. 65 (2010) 2416–2422.

[80] F. Rozgonyi, D. Szabo, B. Kocsis, E. Ostorházi, G. Abbadessa, M. Cassone, J. D. Wade, L. Otvos Jr., The antibacterial effect of a proline-rich antibacterial peptide A3-APO, Curr. Med. Chem. 16 (2009) 3996–4002.

[81] L. Holfeld, D. Knappe, R. Hoffmann, Proline-rich antimicrobial peptides show a long-lasting post-antibiotic effect on *Enterobacteriaceae* and *Pseudomonas aeruginosa*, Antimicrob. Agents Chemother. 73 (2017) 933–941.

[82] D. Knappe, R. Schmidt, K. Adermann, R. Hoffmann, Continuous subcutaneous delivery of proline-rich antimicrobial peptide Api137 provides superior efficacy to intravenous administration in a mouse infection model, Front. Microbiol. (2019).
[83] N.R. Soman, G.M. Lanza, J.M. Heuser, P.H. Schlesinger, S.A. Wickline, Synthesis and characterization of stable fluorocarbon nanostructures as drug delivery vehicles for cytolytic peptides, Nano Lett. 8 (2008) 1131–1136.
[84] V. Scasnar, J.E. van Lier, The use of SEP-PAK SI cartridges for the preparation of gallium chloride from the citrate solution, Eur. J. Nucl. Med. 20 (1993) 273.
[85] U.K. Laemmli, Cleavage of structural proteins during the assembly of the head of bacteriophage T4, Nature 227 (1970) 680–685.
[86] M.C. Goorden, F. van der Have, R. Kreuger, R.M. Ramakers, B. Vastenhouw, J. P. Burbach, J. Booij, C.F. Molthoff, F.J. Beekman, VECTor: a Preclinical imaging system for simultaneous submillimeter SPECT and PET, J. Nucl. Med. 54 (2013) 306–312.
[87] O. Ivashchenko, F. van der Have, M.C. Goorden, R.M. Ramakers, F.J. Beekman, Ultra-high-sensitivity submillimeter mouse SPECT, J. Nucl. Med. 56 (2015) 470–475.
[88] A.M. Loening, S.S. Gambhir, AMIDE: a free software tool for multimodality medical image analysis, Mol. Imag. 2 (2003) 131–137.
[89] X. Zhang, X. Xie, D. Qu, J. Ning, H. Zhou, J. Pan, G. Yang, Determining organ dose conversion coefficients for external neutron irradiation by using a voxel mouse model, J. Radiat. Res. 57 (2016) 182–188.
[90] A.D. Martin, M.Z. Daniel, D.T. Drinkwater, J.P. Clarys, Adipose tissue density, estimated adipose lipid fraction and whole body adiposity in male cadavers, Int. J. Obesity Related Metab. Disorders: J. Int. Assoc. Study Obesity 18 (1994) 79–83.
[91] A.C. Riches, J.G. Sharp, D.B. Thomas, S.V. Smith, Blood volume determination in the mouse, J. Physiol. 228 (1973) 279–284.
[92] E. Silverstein, Urine specific gravity and osmolality in inbred strains of mice, J. Appl. Physiol. 16 (1961) 194–196.
[93] The Mouse in Biomedical Research, Academic Press, Burlington, 2007.
[94] B. Davies, T. Morris, Physiological parameters in laboratory animals and humans, Pharm. Res. 10 (1993) 1093–1095.
[95] Y. Zhang, M. Huo, J. Zhou, S. Xie, PKSolver: An add-in program for pharmacokinetic and pharmacodynamic data analysis in Microsoft Excel, Comput. Methods Programs Biomed. 99 (2010) 306–314.